Geophysical Journal International

Geophys. J. Int. (2023) **232,** 2205–2230
Advance Access publication 2022 October 29
GJI Geodynamics and Tectonics

https://doi.org/10.1093/gji/ggac428

A coupled model for phase mixing, grain damage and shear localization in the lithosphere: comparison to lab experiments

David Bercovici,[1] Elvira Mulyukova,[2] Jennifer Girard[1] and Philip Skemer[3]

[1] *Department of Earth & Planetary Sciences, Yale University, New Haven, CT* 06520*, USA. E-mail: david.bercovici@yale.edu*
[2] *Department of Earth & Planetary Sciences, Northwestern University, Evanston, IL* 60208*, USA*
[3] *Department of Earth & Planetary Sciences, Washington University in St. Louis, St Louis, MO* 63105*, USA*

Accepted 2022 October 24. Received 2022 October 12; in original form 2022 June 6

SUMMARY

The occurrence of plate tectonics on Earth is rooted in the physics of lithospheric ductile weakening and shear-localization. The pervasiveness of mylonites at lithospheric shear zones is a key piece of evidence that localization correlates with reduction in mineral grain size. Most lithospheric mylonites are polymineralic and the interaction between mineral phases, such as olivine and pyroxene, especially through Zener pinning, impedes normal grain growth while possibly enhancing grain damage, both of which facilitate grain size reduction and weakening, as evident in lab experiments and field observations. The efficacy of pinning, however, relies on the mineral phases being mixed and dispersed at the grain scale, where well-mixed states lead to greater mylonitization. To model grain mixing between different phases at the continuum scale, we previously developed a theory treating grain-scale processes as diffusion between phases, but driven by imposed compressive stresses acting on the boundary between phases. Here we present a new model for shearing rock that combines our theory for diffusive grain mixing, 2-D non-Newtonian flow and two-phase grain damage. The model geometry is designed specifically for comparison to torsional shear-deformation experiments. Deformation is either forced by constant velocity or constant stress boundary conditions. As the layer is deformed, mixing zones between different mineralogical units undergo enhanced grain size reduction and weakening, especially at high strains. For constant velocity boundary experiments, stress drops towards an initial piezometric plateau by a strain of around 4; this is also typical of monophase experiments for which this initial plateau is the final steady state stress. However, polyphase experiments can undergo a second large stress drop at strains of 10–20, and which is associated with enhanced phase mixing and resultant grain size reduction and weakening. Model calculations for polyphase media with grain mixing and damage capture the experimental behaviour when damage to the interface between phases is moderately slower or less efficient than damage to the grain boundaries. Other factors such as distribution and bulk fraction of the secondary phase, as well as grain-mixing diffusivity also influence the timing of the second stress drop. For constant stress boundary conditions, the strain rate increases during weakening and localization. For a monophase medium, there is theoretically one increase in strain rate to a piezometric steady state. But for the polyphase model, the strain rate undergoes a second abrupt increase, the timing for which is again controlled by interface damage and grain mixing. The evolution of heterogeneity through mixing and deformation, and that of grain size distributions also compare well to experimental observations. In total, the comparison of theory to deformation experiments provides a framework for guiding future experiments, scaling microstructural physics to geodynamic applications and demonstrates the importance of grain mixing and damage for the formation of plate tectonic boundaries.

Key words: Dynamics of lithosphere and mantle; Mechanics theory and modelling; Rheology: crust and lithosphere; Grain size evolution; Mylonites.

1 INTRODUCTION

Strain localization and ductile shear zones are a key feature of tectonic deformation on Earth (Poirier 1980; Bercovici & Karato 2003). Their most prominent expression is in the formation of weak plate tectonic boundaries, which extend across the entire depth of the strong lithosphere (see Bercovici *et al*. 2015; Mulyukova & Bercovici 2019, for recent reviews). While there are several possible physical mechanisms for such localization, mylonites in particular are considered a 'smoking gun' for the role of grain size in lithospheric localization. Mylonites are by definition metamorphic rocks whose diminutive grain size is correlated with extensive deformation, and which are pervasive at many deformation belts and plate boundaries (e.g. White *et al.* 1980; Jin *et al.* 1998; Furusho & Kanagawa 1999; Warren & Hirth 2006; Skemer *et al.* 2010; Linckens *et al.* 2011; Hansen *et al.* 2013). Physically, the coupling of deformation induced grain size reduction with grain size-sensitive creep can provide the requisite positive feedback for localization, whereby deformation causes weakening, which focusses deformation, which enhances weakening and so on.

Lithospheric mylonitization appears prominent where mineral phases mix with each other (e.g. Herwegh *et al.* 2011; Linckens *et al.* 2011, 2015). Phase mixing, in principle, promotes Zener pinning of one phase against the other, that is grains (or parcels of grains) of one phase block grain-boundary migration of the other phase; this retards grain growth and theoretically facilitates grain damage and grain size reduction via dynamic recrystallization (DRX) by enhancing grain-boundary distortion (see Bercovici & Ricard 2012; Mulyukova & Bercovici 2019). In a monophase medium, without phase mixing and pinning and undergoing either diffusion or dislocation creep, the positive feedback leading to localization is lacking, since DRX occurs in conjunction with dislocation creep, which is not grain size sensitive. Moreover, unimpeded grain-boundary migration and grain growth in monophase media leads to rapid rheological healing. A positive localizing feedback might be provided for monophase media via dislocation accommodated grain-boundary sliding or disGBS, although this is limited to a narrow range of conditions in stress, grain size and temperatures (see Hirth & Kohlstedt 1995; Hansen *et al.* 2011), and is generally accompanied by other parallel deformation mechanisms (see Skemer & Hansen 2016, fig. 5). Whether disGBS occurs in fine-grain mylonites—ultramylonites—is unclear since they lack the crystal preferred orientation that is associated with dislocation creep (e.g. see McNamara *et al.* 2001, 2002, and references therein). But even with mylonitization being promoted by Zener pinning in a polyminerallic medium, if the phases remain unmixed and reside as large isolated monophase tectonites, then the requisite pinning is inconsequential. Therefore, the mixing of phases during deformation is also important for a shear localizing feedback.

The process of phase mixing, and its effect on the rheological behaviour of rocks, have been the subject of various laboratory, field and theoretical studies (Bercovici & Ricard 2016; Bercovici & Skemer 2017; Cross & Skemer 2017; Tasaka *et al.* 2017a, b; Bercovici & Mulyukova 2018; Cross *et al.* 2020; Tasaka *et al.* 2020; Wiesman *et al.* 2018; Bercovici & Mulyukova 2021). At higher pressures representative of the mid and lower lithosphere, where cavitation is unlikely, mixing is probably diffusion limited. In particular, Bercovici & Skemer (2017) hypothesized that grain mixing occurs mechanically in which pressure gradients drive grains of one phase along the grain boundaries of the other phase, and transport is limited by diffusion creep. Tasaka *et al.* (2017b) proposed that mixing proceeds by the dissolution and chemical diffusion of one phase's major elements (typically the metal oxide unit, such as MgO) and their precipitation at the other phase's grain-boundary junctions that are in tension. In either case, mixing between phases appears to be driven along compressive stress directions that are normal to the interface between mineral phases. These mechanisms are hard to distinguish, but can be treated with a generic theory for stress driven diffusive mixing.

Here we use our model of diffusive grain mixing and damage (Bercovici & Mulyukova 2018, 2021). We examine phase mixing and grain damage in the context of a deforming and localizing medium relevant to ductile shear zones and torsional deformation experiments with which we can compare our theory. Although the driving conditions at the shear-zone boundaries are simple and unidirectional, the medium's properties—its phase distribution, grain size and viscosity—are heterogeneous, hence the flow field is likewise heterogeneous and 2-D, with induced small scale vortices and localized shear. We test two classical boundary conditions for forcing of the system, that is imposed fixed velocity and imposed fixed shear stress. The former is applicable to lab experiments as well as tectonic environments wherein the velocity is determined by a distal force balance (e.g. ductile shear at a strike-slip shear zone but where the plate velocity is dictated by subduction at some other location). The latter, fixed-stress, condition is relevant for tectonic environments where the motion is dictated by the force balance proximally or locally, at the shear zone itself (e.g. within a subducting slab).

The full model involves a coupled system, including non-Newtonian flow and deformation in two dimensions, evolution of mineral phase fractions through advection and stress-driven grain-scale diffusion, and grain size evolution through coarsening and damage in two-phases with Zener pinning. We outline and develop the full model here (the numerical solution of which is deferred to the Appendix), after which we provide a quantitative comparison between model results and selected torsional experiments in polyphase media.

2 THEORY

2.1 Diffusive grain mixing

We follow the grain-mixing diffusion model of Bercovici & Mulyukova (2018), but with the update by Bercovici & Mulyukova (2021, SI). Specifically, grain-scale mixing of juxtaposed phases under deformation occurs by grains of one phase migrating along the other phase's grain boundaries either mechanically (Bercovici & Skemer 2017) or by dissolution (Tasaka *et al.* 2017b); the resulting mixing of phases is modelled as effective chemical diffusion in a multicomponent system but where diffusive transport occurs along the compressive stress direction. In

the experiments, phase mixing is manifest as small (typically recrystallized) grains of one phase residing at the grain-boundary triple or quadruple junctions of the other phase's grain boundaries. In the model mixing is quantified by the volume fraction of a given phase, and the area density of the interface between phases, or more or less equivalently the interface curvature. Unlike the two-phase grain-damage theory of Bercovici & Ricard (2012), the mineralogical phases, for example olivine and pyroxene, have different velocity vectors $\mathbf{v}_i$ (nominally $i = 1$ represents the minor phase such as pyroxene while $i = 2$ is the major phase such as olivine), since the phases have relative velocities due to mixing. This velocity is separated into a volume average component $\mathbf{v}$ experienced by both phases, and the velocities of each phase relative to this mean flow, denoted by $\mathbf{u}_i$; in total

$$\mathbf{v}_i = \mathbf{v} + \mathbf{u}_i \quad \text{where} \quad \mathbf{v} = \sum_i \phi_i \mathbf{v}_i \quad \text{and thus} \quad \sum_i \phi_i \mathbf{u}_i = 0, \tag{1}$$

where ϕ_i is the volume fraction of phase i in which $\sum_i \phi_i = 1$. Mixing between phases along grain-boundaries is mathematically treated as a diffusive flux, which is dependent on compositional gradients, that is on gradients in the volume fraction of the mineralogical components ϕ_i:

$$\mathbf{u}_i = -\underline{\mathbf{K}}_i \cdot \nabla \phi_i, \tag{2}$$

where $\underline{\mathbf{K}}_i$ is a grain-diffusivity tensor (with standard units of diffusivity of $\mathrm{m}^2\,\mathrm{s}^{-1}$). The relation $\sum_i \phi_i \mathbf{u}_i = 0$ is most simply satisfied by assuming that

$$\underline{\mathbf{K}}_i = (1 - \phi_i)\underline{\boldsymbol{K}}, \tag{3}$$

where $\underline{\boldsymbol{K}}$ is common to both phases, and while the dependence on $1 - \phi_i$ is mathematically required, it is physically sensible since diffusivity of one phase depends on the presence of the other phase (see Bercovici & Mulyukova 2018, for further discussion). Conservation of mass with incompressible phases is given by

$$\frac{\partial \phi_i}{\partial t} + \nabla \cdot (\phi_i \mathbf{v}_i) = 0 \tag{4}$$

whose sum over i also implies $\nabla \cdot \mathbf{v} = 0$, and given eqs (1)–(3), leads to an advection–diffusion equation for the phases

$$\frac{\partial \phi}{\partial t} + \mathbf{v} \cdot \nabla \phi = \nabla \cdot (\phi(1 - \phi)\underline{\boldsymbol{K}} \cdot \nabla \phi), \tag{5}$$

where $\phi_1 \equiv \phi$, $\phi_2 \equiv 1 - \phi$, and hence we drop the subscript i since using either $i = 1$ or 2 leads to the same equation for ϕ. Although the phases have relative velocities $\mathbf{u}_i$ due to mixing, these velocities are already governed by a flow law (eq. 2) and thus not by the macroscopic flow laws of momentum conservation and constitutive relations (see Section 2.2); moreover, $\mathbf{u}_i$ is assumed to be much smaller than the mean velocity $\mathbf{v}$ and negligible in the macroscopic flow laws and advection operators (see Bercovici & Mulyukova 2018).

The diffusive flux of grain migration is assumed to depend on mechanical stress, and the tensorial property of $\underline{\boldsymbol{K}}$ is dictated by the stress tensor. But since $\underline{\boldsymbol{K}}$ is common to both phases, we assume it is related to the mean, or volume averaged stress $\bar{\underline{\boldsymbol{\tau}}} = \sum_i \phi_i \underline{\boldsymbol{\tau}}_i$, where $\underline{\boldsymbol{\tau}}_i$ is the stress in phase i. However, since we refer to stress in multiple forms, that is stress per phase, mean normal stress, mean shear stress, mean invariant stress and mean compressive and tensile stresses, we attempt to reduce the notational burden and drop the bar on the mean stress (just as we did with mean velocity $\mathbf{v}$) and define $\underline{\boldsymbol{\tau}} \equiv \bar{\underline{\boldsymbol{\tau}}}$. Thus if stress has a subscript i, as in $\underline{\boldsymbol{\tau}}_i$, it is per phase, otherwise, it is the volume average over phases, even if the subscripts are N, S, C, etc.

The dependence of diffusive grain flux on stress occurs because grains of one phase migrate along the other phase's grain-boundaries antiparallel to the compressive stress directions and perpendicular to tensile stress directions. Diffusivity thus depends on how much the principal compressive stress is normal to the interface between phases, which is represented in the continuum mixture by $\nabla\phi$. Tensile stress acting normal to the interface cannot drive mixing of one phase into the other, since it would only drive mean motion along the boundary and not allow mixing. Only the compressive component of the stress tensor $\underline{\boldsymbol{\tau}}_\mathrm{c}$ acting on the interface between phases drives mixing, that is where $\underline{\boldsymbol{\tau}}_\mathrm{c} \cdot \nabla\phi \neq 0$. The compressive components of the stress tensor can be isolated considering the eigenvalues and eigenvectors of any stress tensor. The compressive components are the negative eigenvalues of the tensor times a dyadic product of the associated eigenfunctions. Our model is in two dimensions, in the x–z plane, thus we consider the 2-D stress tensor

$$\underline{\boldsymbol{\tau}} = \begin{bmatrix} \tau_\mathrm{N} & \tau_\mathrm{S} \\ \tau_\mathrm{S} & -\tau_\mathrm{N} \end{bmatrix} \equiv \tau_\mathrm{N}(\hat{\mathbf{x}}\hat{\mathbf{x}} - \hat{\mathbf{z}}\hat{\mathbf{z}}) + \tau_\mathrm{S}(\hat{\mathbf{x}}\hat{\mathbf{z}} + \hat{\mathbf{z}}\hat{\mathbf{x}}), \tag{6}$$

where $\hat{\mathbf{x}}$ and $\hat{\mathbf{z}}$ are unit vectors, and τ_N and τ_S are the mean normal and shear stresses, respectively. The principal stresses or eigenvalues λ of this tensor are

$$\lambda = \pm\sqrt{\tau_\mathrm{N}^2 + \tau_\mathrm{S}^2} = \pm\sqrt{\tfrac{1}{2}\underline{\boldsymbol{\tau}} : \underline{\boldsymbol{\tau}}} = \pm\tau, \tag{7}$$

where τ^2 is the 2nd invariant of the stress tensor. The unit vector for the compressive stress direction $\hat{\mathbf{n}}$ is the eigenvector associated with the eigenvalue $\lambda = -\tau$, and given by

$$\hat{\mathbf{n}} = \pm\frac{\tau_\mathrm{S}\hat{\mathbf{x}} - (\tau + \tau_\mathrm{N})\hat{\mathbf{z}}}{\sqrt{2\tau(\tau + \tau_\mathrm{N})}}. \tag{8}$$

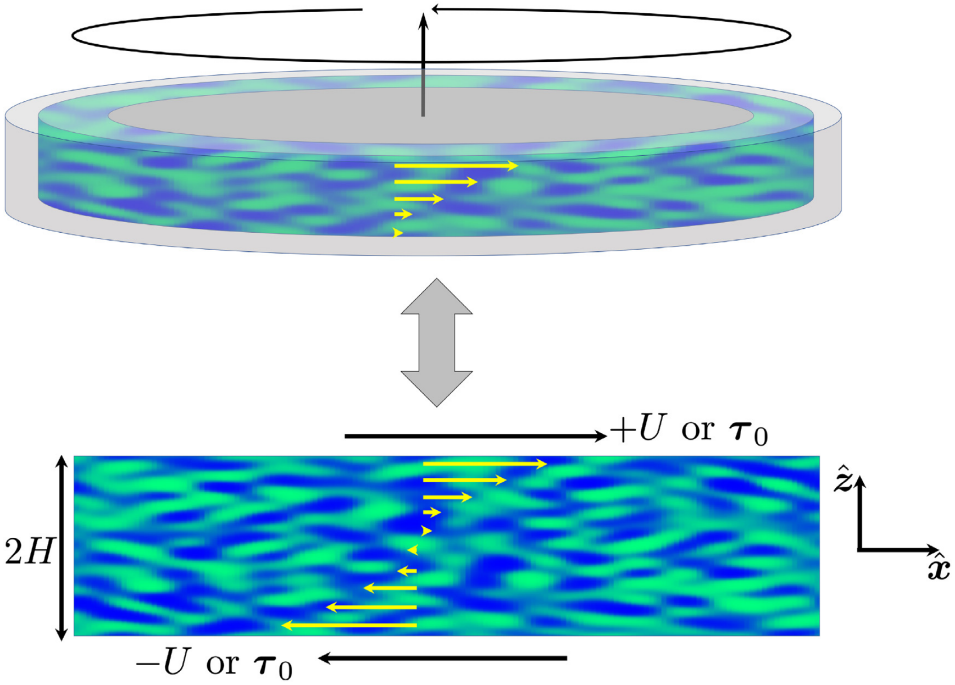

Figure 1. Sketch of a deformation experiment of a thin cylindrical annulus in torsion (top panel), and 2-D Cartesian analogue of a simple-shear model geometry (bottom panel). The heterogeneous green and blue medium represents a mixture of mineral phases like olivine and pyroxene (or ferroperriclase). (The sample annulus for the torsion experiments is typically embedded in soft material like nickel at its inner and outer radial boundaries, indicated by a grey medium, in which the outer bounding medium is rendered semi-transparent.) The model layer is of thickness $2H$ (with a vertical domain given by $z \in [-H, H]$) and the top and bottom boundaries are either at fixed horizontal velocities $\pm U$ or at an imposed fixed horizontal shear stress τ_0.o

The compressive component of the stress tensor is thus

$$\underline{\boldsymbol{\tau}}_c = -\tau\hat{\mathbf{n}}\hat{\mathbf{n}} = -\frac{1}{2}\begin{bmatrix}\tau-\tau_N & -\tau_S\\ -\tau_S & \tau+\tau_N\end{bmatrix} = -\frac{1}{2}\left[(\tau-\tau_N)\hat{\mathbf{x}}\hat{\mathbf{x}} - \tau_S(\hat{\mathbf{x}}\hat{\mathbf{z}}+\hat{\mathbf{z}}\hat{\mathbf{x}}) + (\tau+\tau_N)\hat{\mathbf{z}}\hat{\mathbf{z}}\right]. \tag{9}$$

The effective diffusivity tensor is

$$\underline{\boldsymbol{K}} = -\mathcal{K}\underline{\boldsymbol{\tau}}_c \tag{10}$$

and using eq. (9), the mass conservation eq. (5) becomes

$$\begin{aligned}\frac{D\phi}{Dt} &= -\boldsymbol{\nabla}\cdot\left(\phi(1-\phi)\mathcal{K}\underline{\boldsymbol{\tau}}_c\cdot\boldsymbol{\nabla}\phi\right)\\ &= \frac{1}{2}\left[\frac{\partial}{\partial x}\left(\chi(\tau-\tau_N)\frac{\partial\phi}{\partial x}\right)+\frac{\partial}{\partial z}\left(\chi(\tau+\tau_N)\frac{\partial\phi}{\partial z}\right)-\frac{\partial}{\partial x}\left(\chi\tau_S\frac{\partial\phi}{\partial z}\right)-\frac{\partial}{\partial z}\left(\chi\tau_S\frac{\partial\phi}{\partial x}\right)\right],\end{aligned} \tag{11}$$

where $\frac{D}{Dt} = \frac{\partial}{\partial t} + \mathbf{v}\cdot\boldsymbol{\nabla}$ and we introduce $\chi = \phi(1-\phi)\mathcal{K}$ to streamline notation. We further simplify and generalize the micromechanical model for mixing from Bercovici & Skemer (2017) and Bercovici & Mulyukova (2018) by assuming that

$$\mathcal{K} = \omega B\,\bar{R}^{2-m}, \tag{12}$$

where B is the diffusion creep compliance as a representative of grain size dependent diffusion (since there are no comprehensive measurements for pyroxene diffusion creep, we use the olivine values for both phases; *cf.* Bruijn & Skemer 2014; Zhang *et al.* 2017), $\bar{R} = \sum_i \phi_i R_i$ is the average grain size common to both phases, and the factor ω can be calibrated to ensure that mixing diffusion is comparable to the atomic diffusion of major elements like oxygen and silicon (see also Bercovici & Mulyukova 2021). However, the physics of grain-scale mixing is still an active area of research, and these relations are simple approximations given the current state of knowledge. We thus explore a range of values for ω in our comparison to laboratory experiments, effectively through the dimensionless parameter α introduced later (see Section 2.5).

2.1.1 Grain mixing diffusion boundary conditions

In this paper, we focus on comparison to torsional laboratory experiments, in which the rock layer is deformed by rigid, impermeable horizontal plates at positions $z = \pm H$ (see Fig. 1). We assume the diffusive flux of grains is zero through the top and bottom boundaries; with this flux

given by eq. (2) and the diffusivity tensor given by eq. (10) we arrive at

$$(\underline{\boldsymbol{\tau}}_{\mathrm{c}} \cdot \nabla\phi) \cdot \hat{\mathbf{z}} = 0 \ \text{ at } \ z = \pm H \tag{13}$$

and given our 2-D system this yields

$$(\tau + \tau_{\mathrm{N}})\frac{\partial \phi}{\partial z} - \tau_{\mathrm{S}}\frac{\partial \phi}{\partial x} = 0 \ \text{ at } \ z = \pm H. \tag{14}$$

2.2 Model geometry, kinematics and dynamics

We seek to model a laboratory deformation experiment in torsion or simple shear. As noted already, the model domain is 2-D in the x–z plane, and, in order to simply represent a torsion apparatus, it is periodic in the horizontal x direction over a length $2L$, and bounded on the top and bottom at $z = \pm H$, where $2H$ is the width of the shearing layer. Using a 2-D Cartesian domain assumes the cylindrical sample in torsion is very thin in the radial direction and free-slip on the vertical cylindrical surfaces (Fig. 1). In the relevant torsional laboratory experiments, the thin annular samples are bounded at their inner and outer cylindrical surfaces by a weaker material, such as nickel (e.g. see Hansen *et al.* 2012).

To zeroth order, the dominant flow field is that of 1-D simple shear

$$\mathbf{v}_0 = U\frac{z}{H}\hat{\mathbf{x}}, \tag{15}$$

where U is the speed of the horizontal boundaries at $z = \pm H$, which are moving in opposite directions. With viscosity variations due to heterogeneity in phase fraction and grain size, there are 2-D velocity fluctuations in addition to the background flow. The total velocity, including the background flow and fluctuations, is

$$\mathbf{v} = u\hat{\mathbf{x}} + w\hat{\mathbf{z}} \tag{16}$$

which is solenoidal since

$$\nabla \cdot \mathbf{v} = 0. \tag{17}$$

A 2-D solenoidal velocity field is given by

$$\mathbf{v} = \nabla \times (\Psi\hat{\mathbf{y}}). \tag{18}$$

where $\hat{\mathbf{y}}$ is the unit vector out of the plane, and Ψ is the stream function, which is dependent on x, z and time t only.

One of the key metrics of localized shear is concentrated bands of vorticity in the y direction, defined as $\Omega = \hat{\mathbf{y}} \cdot \nabla \times \mathbf{v}$. Given eq. (18), the vorticity and toroidal potential are related by

$$\nabla^2\Psi = -\Omega. \tag{19}$$

However, Ω itself is determined by the momentum equation, which we treat next.

The conservation of momentum in creeping two-phase flow with grained phases was prescribed by Bercovici & Ricard (2012) and, in the limit where the two macroscopic phase velocities are approximately the same (i.e. $\mathbf{v}_i \approx \mathbf{v}$, since we assume $|\mathbf{u}_i| \ll |\mathbf{v}|$), the summed momentum equation is sufficient and is given by

$$0 = \nabla\Pi + \nabla \cdot \underline{\boldsymbol{\tau}} + \rho\mathbf{g} + \nabla(\gamma_I\mathcal{A}), \tag{20}$$

where the pressure Π and density ρ are, like stress $\underline{\boldsymbol{\tau}}$, volume averaged over the two phases; $\mathbf{g}$ is gravitational acceleration; γ_{I} is the surface tension on the interface between phases and $\mathcal{A}$ is the interface density (interface area per unit volume). The mean stress tensor is

$$\underline{\boldsymbol{\tau}} = \mu\left(\nabla\mathbf{v} + [\nabla\mathbf{v}]^{\mathrm{t}}\right), \tag{21}$$

where μ is the volume average of the viscosities in each phase μ_i, the rheological model of which will be discussed below in Section 2.3. Substituting eq. (21) into eq. (20) and taking $\hat{\mathbf{y}} \cdot \nabla\times$ of the resulting equation leads to an elliptic equation for the vorticity Ω

$$\mu\nabla^2\Omega = -2\nabla\mu \cdot \nabla\Omega + \Delta^*\mu\Delta^*\Psi + 4\tfrac{\partial^2\mu}{\partial x\partial z}\tfrac{\partial^2\Psi}{\partial x\partial z}, \tag{22}$$

where we define the differential operator (Bercovici 1993)

$$\Delta^* = \frac{\partial^2}{\partial x^2} - \frac{\partial^2}{\partial z^2}. \tag{23}$$

Deformation is driven by imposed velocities or stresses at the top and bottom boundary, and these determine the zeroth order velocity (eq. 15), as well as the zeroth order vorticity and stream function:

$$\Omega_0 = \tfrac{U}{H} \tag{24a}$$

$$\Psi_0 = -\tfrac{Uz^2}{2H} = -\Omega_0\tfrac{z^2}{2}. \tag{24b}$$

The total stream function, velocity and vorticity are thus

$$\Psi = \Psi_0 + \psi = -\Omega_0 \tfrac{z^2}{2} + \psi \tag{25a}$$

$$\mathbf{v} = \mathbf{v}_0 + \boldsymbol{\nabla} \times (\psi \hat{\mathbf{y}}) = \Omega_0 z \hat{\mathbf{x}} + \boldsymbol{\nabla} \times (\psi \hat{\mathbf{y}}) \tag{25b}$$

$$\Omega = \Omega_0 + \omega \tag{25c}$$

which implies that, with (eq. 19),

$$\nabla^2 \psi = -\omega. \tag{26}$$

We can further separate the viscosity relative to a uniform background μ_0 such that

$$\mu = \mu_0 + \upmu(x, z, t), \tag{27}$$

where we typically choose $\mu_0 = \max(\mu)$. In this case eq. (22) becomes

$$\nabla^2 \omega = -\mathcal{M} \nabla^2 \omega - 2 \boldsymbol{\nabla} \mathcal{M} \cdot \boldsymbol{\nabla} \omega + \Delta^* \mathcal{M} \, (\Omega_0 + \Delta^* \psi) + 4 \frac{\partial^2 \mathcal{M}}{\partial x \partial z} \frac{\partial^2 \psi}{\partial x \partial z}, \tag{28}$$

where $\mathcal{M} = \upmu / \mu_0$ is a normalized viscosity anomaly. Viscosity variability is dictated by the rheological model for the medium, which is discussed in Section 2.3.

2.2.1 Kinematic and dynamic boundary conditions

The top and bottom horizontal boundaries of the deforming layer are either of fixed horizontal velocity or with a fixed imposed shear stress. Regardless of whether the boundaries are fixed velocity or fixed stress, we can assume they are impermeable in which case $w = 0$ at the top and bottom, and thus

$$\frac{\partial \psi}{\partial x} = 0 \;\text{ at }\; z = \pm H. \tag{29}$$

For fixed velocity or no-slip boundaries, the horizontal velocity $u = \pm U$ at the top and bottom, which implies that

$$\frac{\partial \psi}{\partial z} = 0 \;\text{ at }\; z = \pm H. \tag{30}$$

Imposing eq. (30) in addition to eq. (29) means that all four boundary conditions are applied to ψ, in which case eqs (26) and (28) should be consolidated into a single 4th order biharmonic equation for ψ (see Section A1, for further discussion).

For fixed stress conditions, we assume a lateral shear stress τ_0 is imposed at the top and bottom such that

$$\mu \frac{\partial u}{\partial z} = \mu \Omega = \mu \, (\Omega_0 + \omega) = \tau_0 \;\text{ at }\; z = \pm H, \tag{31}$$

where we have already assumed $\partial w / \partial x = 0$ at the boundaries given eq. (29). The above equation is a boundary condition on Ω, or ω, which can be applied to eq. (28). However, to simplify the boundary condition further, we invoke eq. (27) and prescribe the zeroth order boundary velocity as $U = H \tau_0 / \mu_0$, and the zeroth order background vorticity as $\Omega_0 = \tau_0 / \mu_0$, for which eq. (31) yields

$$\begin{aligned} &\upmu \Omega_0 \;\; + (\mu_0 + \upmu) \omega = 0 \;\text{ at }\; z = \pm H \\ &\quad \Rightarrow \omega = -\tfrac{\mathcal{M}}{1+\mathcal{M}} \Omega_0 \;\text{ at }\; z = \pm H. \end{aligned} \tag{32}$$

However, the background viscosity μ_0 can change as the system, especially grain size, evolves and thus neither the zeroth order boundary velocities $\pm U$ nor background vorticity Ω_0 are constant in time for cases with the fixed stress boundary condition.

2.3 Rheology

Each mineralogical phase has, in principle, a unique and non-uniform grain size distribution. Grains in these distributions are assumed to predominantly undergo either diffusion or dislocation creep depending on whether they are, respectively, smaller or bigger than a critical size—called the field-boundary grain size—defining the transition between creep mechanisms (e.g. see Rozel *et al.* 2011; Bercovici & Ricard 2012, appendix F.7). The strain rate tensor in either phase, averaged over the grain size distribution, yields a composite rheological law given by

$$\underline{\dot{\boldsymbol{\epsilon}}} = \tfrac{1}{2} (\boldsymbol{\nabla} \mathbf{v} + [\boldsymbol{\nabla} \mathbf{v}]^{\mathrm{t}}) = \left(A_i \tau_i^{n-1} + \frac{B_i}{R_i^m} \right) \underline{\boldsymbol{\tau}}_i \tag{33}$$

assuming that stress is the same for all grains of like phase i within a small volume; note that while the averaged strain rate is the same for both phases in the parcel (since they have the same macroscopic velocity), their stresses can differ. In eq. (33), $\tau_i = \sqrt{\tfrac{1}{2} \underline{\boldsymbol{\tau}}_i : \underline{\boldsymbol{\tau}}_i}$ is the

square-root of the second stress invariant for phase i; R_i is the characteristic or mean grain size for phase i; A_i and B_i are the dislocation and diffusion creep compliances for phase i, respectively; n is the dislocation-creep power-law index (experimental values for olivine imply $n = 3.5$); m is the grain size dependence index that is typically 2 for diffusion through grains (Nabarro–Herring creep) and 3 for diffusion along grain boundaries (Coble creep); the exponents n and m are assumed the same for both phases for simplicity although that assumption is easily relaxed. The composite rheology eq. (33) implies that the transition from dislocation-creep dominated to diffusion-creep dominated deformation occurs for the macroscopic parcel at the field-boundary grain size

$$R_f = \left(\frac{B_i}{A_i \tau_i^{n-1}}\right)^{1/m}. \tag{34}$$

Thus, a parcel whose grain size distribution has a mean size far from R_f will predominantly deform by one creep mechanism or the other. The viscosity of phase i is defined by (see eq. 33)

$$\mu_i = \frac{\tau_i}{2\dot{e}} = \frac{1}{2}\left(A_i \tau_i^{n-1} + \frac{B_i}{R_i^m}\right)^{-1}, \tag{35}$$

where τ_i is the solution to

$$A_i \tau_i^n + \frac{B_i}{R_i^m}\tau_i - \dot{e} = 0 \tag{36}$$

for a given $\dot{e}$ in which, using eq. (25)

$$\dot{e}^2 = \tfrac{1}{2}\underline{\dot{\mathbf{e}}} : \underline{\dot{\mathbf{e}}} = \left(\frac{\partial^2 \psi}{\partial x \partial z}\right)^2 + \frac{1}{4}\left(\Omega_0 + \Delta^* \psi\right)^2. \tag{37}$$

Eq. (36) can be solved exactly for $n = 1$, 2 or 3 (e.g. see Bercovici & Ricard 2012, section 4.1), or numerically otherwise (see A1.1). The mean viscosity is thus

$$\mu = \sum_i \phi_i \mu_i = \sum_i \frac{\phi_i}{2}\left(A_i \tau_i^{n-1} + \frac{B_i}{R_i^m}\right)^{-1} = \frac{\tau}{2\dot{e}}. \tag{38}$$

The viscosity thus depends on the stress or strain rate, and the grain size R_i in phase i whose evolution is discussed in the next section.

Finally, once μ is determined, the normal and shear stresses for the compressive stress used in the grain-diffusion model (eq. 9) can be determined, respectively, as

$$\tau_{\mathrm{N}} = -2\mu \frac{\partial^2 \psi}{\partial x \partial z} \quad \text{and} \quad \tau_{\mathrm{S}} = \mu(\Omega_0 + \Delta^* \psi). \tag{39}$$

The individual phases' stresses τ_i, the mean stress τ, and the normal and shear stresses above, are related according to

$$\tau = \sum_i \phi_i \tau_i = \sqrt{\tau_{\mathrm{N}}^2 + \tau_{\mathrm{S}}^2}. \tag{40}$$

However, note this final relationship between the invariant of the mean stress and the mean of the invariant stresses is strictly only true provided homogenous strain, that is that $\dot{e}$ is the same for both phases.[1]

Finally, we note (and as already stated previously) that because data on pyroxene diffusion creep is non-existent or sparse, olivine values are often used instead. For consistency and simplicity we opt to use the same rheology, that of olivine, for both model phases such that $A_i = A$ and $B_i = B$. The validity of this assumption towards comparison to laboratory experiments is discussed below in Section 3.

2.4 Two-phase grain damage with mixing

The essential tenet of two-phase grain damage is that Zener pinning between phases (wherein the grains of one phase block grain-boundary migration of the other phase) retards healing via grain growth, and facilitates grain damage and comminution via dynamic recrystallization. These processes thus allow grain size to shrink well into the diffusion-creep regime with grain size sensitive viscosity, which promotes a self-softening feedback, and to remain in that regime semi-permanently (see Mulyukova & Bercovici 2019, for recent review and graphical explanation). Zener pinning is only active if the grains of both phases are dispersed or mixed with each other, hence the mixing mechanism discussed above controls where two-phase grain damage can occur (Bercovici & Mulyukova 2018, 2021).

The physics of both grain damage and mixing in two phases is dependent on the representation of the interface between phases (Bercovici *et al*. 2001; Bercovici & Ricard 2012). The density of this interface, that is its area per unit volume in the mixture, is $\mathcal{A} = \eta(\phi)/r$ in which r

[1] In general, $\underline{\boldsymbol{\tau}}_i = 2\mu_i \underline{\dot{\mathbf{e}}}$, from which we find the mean stress $\underline{\boldsymbol{\tau}} = \sum_i \phi_i \underline{\boldsymbol{\tau}}_i = 2\mu \underline{\dot{\mathbf{e}}}$, the scalar invariant of which is $\tau = \sqrt{\tfrac{1}{2}\underline{\boldsymbol{\tau}} : \underline{\boldsymbol{\tau}}} = 2\mu\sqrt{\tfrac{1}{2}\underline{\dot{\mathbf{e}}} : \underline{\dot{\mathbf{e}}}} = 2\mu\dot{e}$. Similarly, the scalar invariant of the stress in phase i is $\tau_i = \sqrt{\tfrac{1}{2}\underline{\boldsymbol{\tau}}_i : \underline{\boldsymbol{\tau}}_i} = 2\mu_i \dot{e}$, the volume averaged of which is $\sum \phi_i \tau_i = 2\mu\dot{e} \equiv \tau$. However these relations would not hold if $\underline{\dot{\mathbf{e}}}$ were unique to each phase.

is the characteristic interface radius of curvature also referred to as interface roughness, and typically $\eta = 3\phi_1\phi_2 = 3\phi(1-\phi)$, which ensures that the interface area vanishes in the limit of $\phi_i \to 0$ or 1 (Bercovici *et al.* 2001, section 2.2). When the phases are unmixed, the interface that separates them is smooth, meaning that it has a large radius of curvature r, and the interface area is minimized. When the phases are well mixed, in which one phase is well dispersed through the other phase, the interface is rougher and has a small radius of curvature r.

The two-phase damage equations describe the coupled evolution between grain sizes in each phase and the interface roughness, all in terms of the competition between healing via surface-tension driven coarsening, and deformationally driven damage and grain comminution. These equations were most recently adapted to include diffusive mixing by Bercovici & Mulyukova (2018, 2021) and appear as

$$\frac{\mathrm{D}r}{\mathrm{D}t} = \frac{\eta G_I}{q r^{q-1}} - \frac{r^2 f_I \eta^\ell}{\gamma_I}\left(2\sum_i \phi_i\left(A_i \tau_i^{n+1} + B\tau_i^2/R_i^m\right) + \phi(1-\phi)\mathcal{K}|\underline{\boldsymbol{\tau}}_c \cdot \nabla\phi|^2\right) \tag{41}$$

$$\frac{\mathrm{D}R_i}{\mathrm{D}t} = \frac{G_i}{p R_i^{p-1}}\mathcal{Z}_i - \frac{\lambda R_i^2 f_G}{3\gamma_i} 2A_i \tau_i^{n+1}\mathcal{Z}_i^{-1}, \tag{42}$$

where G_i and p are the rate and the exponent of grain boundary coarsening, respectively; G_I and q are the analogous rate and exponent of interface coarsening; $\mathcal{Z}_i$ is the Zener pinning factor, to be discussed shortly, and γ_I and γ_i are the interface and the grain boundary surface energies, respectively. The partitioning fractions f_I and f_G determine how much of the deformational work is partitioned into new interface and grain boundary area, respectively (see also Bercovici & Ricard 2016), where the work to produce more grain boundary area is restricted to dislocation creep. The work to produce more interface area is extracted from the total work rate, including that associated with grain-scale mixing, since any mode of deformation will cause interface distortion by stretching, rending or mixing. The range of possible values for f_I and f_G were determined in Bercovici & Ricard (2016) and Mulyukova & Bercovici (2017), by comparing the theoretically predicted steady state grain sizes to the ones reported from experimental (Post 1977; Karato *et al.* 1980; Van der Wal *et al.* 1993; Jung & Karato 2001; Linckens *et al.* 2014) and field data (e.g. Herwegh *et al.* 2011; Linckens *et al.* 2011, 2015) for different stress and temperature conditions. Although the interface surface energy is proportional to $\gamma_1\eta$, we include a factor in the interface damage term $\eta^{\ell+1}$ adjacent to f_I (in which $\ell > 0$) since we expect no interface damage when $\phi = 0$ or 1 hence when $\eta = 0$. As in our previous studies (most recently Bercovici & Mulyukova 2021), the factor $\lambda = 4.95$, but is specific to the assumed lognormal grain size distribution.

The Zener pinning factor $\mathcal{Z}_i$ in eq. (42), which couples the grain size and the interface roughness evolution, is defined as (Bercovici & Ricard 2012):

$$\mathcal{Z}_i = 1 - \mathfrak{c}(1-\phi_i)\left(\frac{R_i}{r}\right)^2, \tag{43}$$

where $\mathfrak{c} = 0.87$, which is associated with the grain size distribution used previously (again, most recently Bercovici & Mulyukova 2021). The relation for the Zener pinning factor eq. (43) can be adjusted to preclude negative values of $\mathcal{Z}_i$, specifically

$$\mathcal{Z}_i = 1 - \tanh\left(\mathfrak{c}(1-\phi_i)\left(\frac{R_i}{r}\right)^2\right) \tag{44}$$

(see Bercovici & Mulyukova 2018, 2021). In total, eqs (41) and (42) show that, in a polymineralic medium, grain damage is expressed in two forms, grain-boundary damage (i.e. reduction in R_i) and interface damage (i.e. reduction in r). These forms of damage are coupled through the influence of the interface between phases via Zener pinning. In particular, the evolution laws for grain sizes in each phase eq. (42) are affected by the interface between the phases in two ways. First, the interface obstructs grain-boundary migration and hence retards grain growth, which is the canonical definition of Zener pinning (e.g. Smith 1948; Hillert 1965, 1988; Manohar *et al.* 1998). The second effect of Zener pinning on grain size evolution, as shown by Bercovici & Ricard (2012), is that, as $\mathcal{Z}_i$ decreases, grain size reduction by damage is amplified (see Bercovici & Ricard 2012; Mulyukova & Bercovici 2019, for further discussion and a graphical explanation). Reduction in r through interface damage causes $\mathcal{Z}_i$ to approach zero, thus impeding grain growth and healing and enhancing grain-boundary damage and grain size reduction. Thus the coupling of grain-boundary and interface damage allows for grain size reduction and grain size sensitive rheology to coexist, providing a positive feedback mechanism for self-weakening of polymineralic rocks. Moreover, the model equations of grain damage with phase mixing posit that grain reduction and weakening depend on the level of mixing between phases. For monomineralic unmixed units, Zener pinning is essentially non-existent and thus weakening and localization is suppressed. However, in zones where the phases mix, Zener pinning is enhanced and weakening and grain size reduction are most profound.

2.5 Dimensionless governing equations

Our dimensional governing equations are (eq. 11) for the evolution of phase volume fraction ϕ; eqs (26) and (28) for stream-function ψ and vorticity ω, which dictate the flow and deformation fields; and eqs (41) and (42) for the evolution of grain sizes in each phase R_i and the roughness of the interface between phases r. The natural geometric scale of the system is set by the layer half-width H, in which case we define $\mathbf{x} = H\mathbf{x}'$ and $\nabla = H^{-1}\nabla'$, where primed quantities are dimensionless, and the vertical domain of the layer is now $z' \in [-1, 1]$. However, the velocity (and hence time), stress (and hence viscosity) and grain size scales are set by the dynamic boundary conditions, that is either by the imposed velocities $\pm U$ at the top and bottom boundaries for the no-slip condition, or a fixed shear stress τ_0 imposed at the top and bottom boundaries. The resulting dimensionless governing equations differ slightly depending on the scales used, although they can be presented in a unified form.

For the no-slip boundaries, the velocity scale is $\tilde{\mathrm{U}} = U$. The stress scale depends on the rheological parameters, A_i, B_i, n, m. Because pyroxene has no widely accepted diffusion creep law, we use the compliance factor $B_i = B_2 = B$ for olivine for both phases, and for consistency do likewise for the dislocation creep factor, thus assume $A_i = A$. Moreover, while A and B are nominally temperature dependent, we prescribe the model to be at a fixed temperature as appropriate for a lab experiment or a given depth (or really isotherm) in the lithosphere. We therefore define the stress scale according to

$$\tilde{\tau} = \left(\frac{U}{2AH}\right)^{1/n} \tag{45}$$

since the zeroth order or background strain rate is $U/(2H)$.

For the fixed shear-stress boundary condition, we define the stress scale as $\tilde{\tau} = \tau_0$, in which case the velocity scale is

$$\tilde{\mathrm{U}} = 2A\tau_0^n H. \tag{46}$$

For either case, time is scaled according to $t = \tilde{\mathrm{t}}t'$, where $\tilde{\mathrm{t}} = H/\tilde{\mathrm{U}}$, and the variables involving flow and deformation are scaled according to

$$(\mathbf{v}, \Psi, \Omega, \dot{e}) = \tilde{\mathrm{U}}(\mathbf{v}', H\Psi', H^{-1}[\Omega', \dot{e}']) \tag{47}$$

and the viscosity μ, and both grain size R_i and interface roughness r are scaled by

$$\tilde{\mu} = \left(2A\tilde{\tau}^{n-1}\right)^{-1} \quad \text{and} \quad \tilde{R} = \left(\frac{B}{A\tilde{\tau}^{n-1}}\right)^{1/m}, \tag{48}$$

respectively. With either boundary condition, the flow eq. (25) can be expressed dimensionlessly as (but dropping the primes)

$$\Psi = -\tfrac{1}{2}\Omega_0 z^2 + \psi \tag{49a}$$

$$\mathbf{v} = \Omega_0 z\hat{\mathbf{x}} + \nabla \times (\psi\hat{\mathbf{y}}) \tag{49b}$$

$$\Omega = \Omega_0 + \omega \tag{49c}$$

in which ψ and ω still obey eqs (26) and (28), but we show them again for completeness:

$$\nabla^2\psi = -\omega \tag{50}$$

$$\nabla^2\omega = -\mathcal{M}\nabla^2\omega - 2\nabla\mathcal{M}\cdot\nabla\omega + \Delta^*\mathcal{M}\,(\Omega_0 + \Delta^*\psi) + 4\tfrac{\partial^2\mathcal{M}}{\partial x\partial z}\tfrac{\partial^2\psi}{\partial x\partial z}, \tag{51}$$

where the definition of $\mathcal{M} = (\mu - \mu_0)/\mu_0 = \mu/\mu_0$ has not changed since it was already a normalized viscosity. The dimensionless boundary conditions now become

$$\frac{\partial\psi}{\partial x} = 0 \text{ and } \left\{\begin{array}{ll} \frac{\partial\psi}{\partial z} = 0 & \text{for fixed velocity, or} \\ \omega = -\frac{\mathcal{M}}{1+\mathcal{M}}\Omega_0 & \text{for fixed stress} \end{array}\right\} \text{ at } z = \pm 1. \tag{52}$$

The dimensionless strain rate invariant is the same as eq. (37):

$$\dot{e}^2 = \left(\frac{\partial^2\psi}{\partial x\partial z}\right)^2 + \frac{1}{4}(\Omega_0 + \Delta^*\psi)^2\,. \tag{53}$$

For all of these equations, Ω_0 has a dual definition depending on the boundary conditions:

$$\Omega_0 = \begin{cases} 1, & \text{for fixed velocity boundaries} \\ 1/\mu_0, & \text{for fixed stress boundaries,} \end{cases} \tag{54}$$

where μ_0 is the maximum viscosity (normalized by $\tilde{\mu}$) at time t. The dimensionless stress invariant in each phase τ_i is the solution to

$$\tau_i^n + \frac{\tau_i}{R_i^m} - 2\dot{e} = 0 \tag{55}$$

and the equation for the mean viscosity and normal and shear stress components do not change from eq. (38)—specifically that $\mu = \tau/(2\dot{e})$—and eq. (39). Note that given the scaling of the systems with either fixed velocity boundaries or fixed stress boundaries, the peak velocities, vorticities, stresses and viscosities will be unity in the initial stages of evolution when $R_i, r \gg 1$. In particular, in the fixed velocity boundary case, the background strain rate is $\dot{e} = 1/2$ which, for large grains, leads to $\tau_i \approx 1$, and thus the velocities, vorticity and viscosities follow as unity also. For the fixed stress boundary case, $\tau_i = 1$, which again leads (for large grains) to $\dot{e} \approx 1/2$ and the other quantities again follow to become unity. Moreover, note that the non-dimensionalizing scale $\tilde{R}$ for grain size R_i and interface roughness r is the field boundary grain size at the characteristic stress $\tilde{\tau}$. The typical dimensionless field-boundary grain size is, therefore, $O(1)$ when the dimensionless stress is also $O(1)$, for example at the initial stages of the simulations. But since stress is variable in space and time, there is no unique field boundary in these cases; indeed, as the stress drops in cases with fixed velocity top and bottom, the field-boundary grain size increases as $\tau^{(1-n)/m}$. Therefore as the dimensionless grain sizes reduce to $O(1)$ and below, they are guaranteed to converge on and even fall below the field boundary.

Table 1. Table of material properties.

Definition	Formula	Amplitude (s^{-1})	Act. energy ($kJ\,mol^{-1}$)	Act. volume ($cm^3\,mol^{-1}$)	Exponent
Dislocation					
Creep Compliance (ol,px)	$A = A_0(\text{MPa})^{-n} e^{-\frac{E_a+PV_a}{\mathbb{R}T}}$	$A_0 = 1.1 \times 10^5$	$E_a = 530$	$V_a = 14$	$n = 3.5$
Diffusion					
Creep Compliance (ol, px)	$B = B_0(\mu\text{m})^m(\text{MPa})^{-1} e^{-\frac{E_b+PV_b}{\mathbb{R}T}}$	$B_0 = 1.5 \times 10^9$	$E_b = 375$	$V_b = 6$	$m = 3$
Grain coarsening rate	$G_i = G_0(\mu\text{m})^p e^{-\frac{E_g}{\mathbb{R}T}}$	$G_0 = 2 \times 10^4$	$E_g = 200$	–	$p = 2$
Interface coarsening rate	$G_I = G_i(\mu\text{m})^{q-p}/100$				$q = 4$

Note: Olivine creep laws from Hirth & Kohlstedt (2003). The same rheological laws are assumed for pyroxene. Grain-growth law from Karato (1989) for olivine. Interface coarsening rate from Bercovici & Ricard (2013). $\mathbb{R} = 8.3144598\ \text{J Mol}^{-1}\ \text{K}^{-1}$ is the gas constant. Pressure is set to 300 MPa as used in the laboratory experiments.

The evolutions laws for ϕ, r and R_i become

$$\frac{\mathrm{D}\phi}{\mathrm{D}t} = \alpha\left[\tfrac{\partial}{\partial x}\left(\chi(\tau-\tau_\mathrm{N})\tfrac{\partial\phi}{\partial x}\right) + \tfrac{\partial}{\partial z}\left(\chi(\tau+\tau_\mathrm{N})\tfrac{\partial\phi}{\partial z}\right) - \tfrac{\partial}{\partial x}\left(\chi\tau_\mathrm{S}\tfrac{\partial\phi}{\partial z}\right) - \tfrac{\partial}{\partial z}\left(\chi\tau_\mathrm{S}\tfrac{\partial\phi}{\partial x}\right)\right] \tag{56}$$

$$\frac{\mathrm{D}r}{\mathrm{D}t} = \tfrac{\eta\mathcal{C}_I}{qr^{q-1}} - \mathcal{D}_I\eta^\ell r^2\tau\left(2\dot{e} + \tfrac{1}{2}\alpha\chi\left[\sqrt{\tau-\tau_\mathrm{N}}\tfrac{\partial\phi}{\partial x} - \sqrt{\tau+\tau_\mathrm{N}}\tfrac{\partial\phi}{\partial z}\right]^2\right) \tag{57}$$

$$\frac{\mathrm{D}R_i}{\mathrm{D}t} = \tfrac{\mathcal{C}_i}{pR_i^{p-1}}\mathcal{Z}_i - \mathcal{D}_i R_i^2\tau_i^{n+1}\mathcal{Z}_i^{-1}, \tag{58}$$

where $\chi = \phi(1-\phi)\bar{R}^{2-m}$ is still a variable function, and the dimensionless governing parameters are

$$\mathcal{C}_i = \frac{G_i\tilde{\mathrm{t}}}{\tilde{R}^p}\ ,\quad \mathcal{C}_I = \frac{G_I\tilde{\mathrm{t}}}{\tilde{R}^q}\ ,\quad \mathcal{D}_i = \frac{\lambda f_G\tilde{R}\tilde{\tau}}{3\gamma_i}\ ,\quad \mathcal{D}_I = \frac{f_I\tilde{R}\tilde{\tau}}{\gamma_I}\ ,\quad \text{and}\ \ \alpha = \frac{\omega B\tilde{R}^{2-m}\tilde{\tau}\tilde{\mathrm{t}}}{H^2} \equiv \omega\frac{\tilde{R}^2}{2H^2}, \tag{59}$$

where again (in summary)

$$(\tilde{\mathrm{U}},\ \tilde{\mathrm{t}},\ \tilde{\tau}) = \begin{cases} \left(U,\ \frac{H}{U},\ \left(\frac{U}{2AH}\right)^{1/n}\right) & \text{for fixed velocity boundaries} \\ \left(2A\tau_0^n H,\ \left(2A\tau_0^n\right)^{-1},\ \tau_0\right) & \text{for fixed stress boundaries.} \end{cases} \tag{60}$$

The final system of dimensionless equations is solved numerically with a semi-spectral (in x) and finite-difference (in z) method for an elongated domain in which $z \in [-1, 1]$ and $x \in [-5, 5]$. The numerical approach is discussed in detail in the Appendix.

3 COMPARISON TO EXPERIMENTS

3.1 Fixed velocity boundaries

We focus here on testing our model against deformation experiments in polyphase synthetic mixtures, as performed by Tasaka *et al.* (2017a, b, 2020) and Wiesman *et al.* (2018). While we make qualitative comparisons to observations of mineralogical phase heterogeneity (e.g. compositional mixing) and microstructure (e.g. grain size distribution), we provide quantitative comparisons to the evolution of stress with strain in the experiments.

As noted by Tasaka *et al.* (2017a), there is a notable difference between stress evolution in monophase experiments (Hansen *et al.* 2012) and that in polyphase ones, provided a sufficiently large fraction of secondary phases (Tasaka *et al.* 2020). For monophase experiments, there is typically a single drop in stress indicative of weakening, from an initial large value at the start of the experiment, to a smaller steady-state stress plateau (Hansen *et al.* 2012). For polyphase experiments, there is a similar initial stress drop and a plateau, but then a second stress drop can occur at large strains of order 10 and greater, and which is attributed to a significant reduction in grain size and second stage of weakening. As shown below, our model is able to capture these stress drops, and we use the relative magnitude and timing for the stress changes to infer some of the lesser known material properties. We note that the experiments of Wiesman *et al.* (2018) show the clearest indication of a second stress drop and associated weakening; the experiments of Tasaka *et al.* (2017a) also demonstrate a second stress drop at large strains, but typically a more gradual one.

We first must evaluate the governing dimensionless numbers that incorporate the properties of the experimental materials (e.g. rheology, grain-growth rate, damage partitioning), as well as the experimental conditions (temperature, deformation rate, etc.). Reasonably constrained properties for olivine, for example for rheological behaviour, are listed in Table 1. However, the properties we consider the least constrained are the damage partitioning fractions f_G and f_I, which have been estimated before using a synthesis of piezometric data and grain-growth laws (Austin & Evans 2007; Rozel *et al.* 2011; Mulyukova & Bercovici 2017). Thus some of our dimensionless numbers are reasonably well constrained (e.g. the grain and interface coarsening numbers $\mathcal{C}_i$ and $\mathcal{C}_I$) and some are less so, such as the grain and interface damage numbers $\mathcal{D}_i$ and $\mathcal{D}_I$ and the grain-mixing diffusivity α.

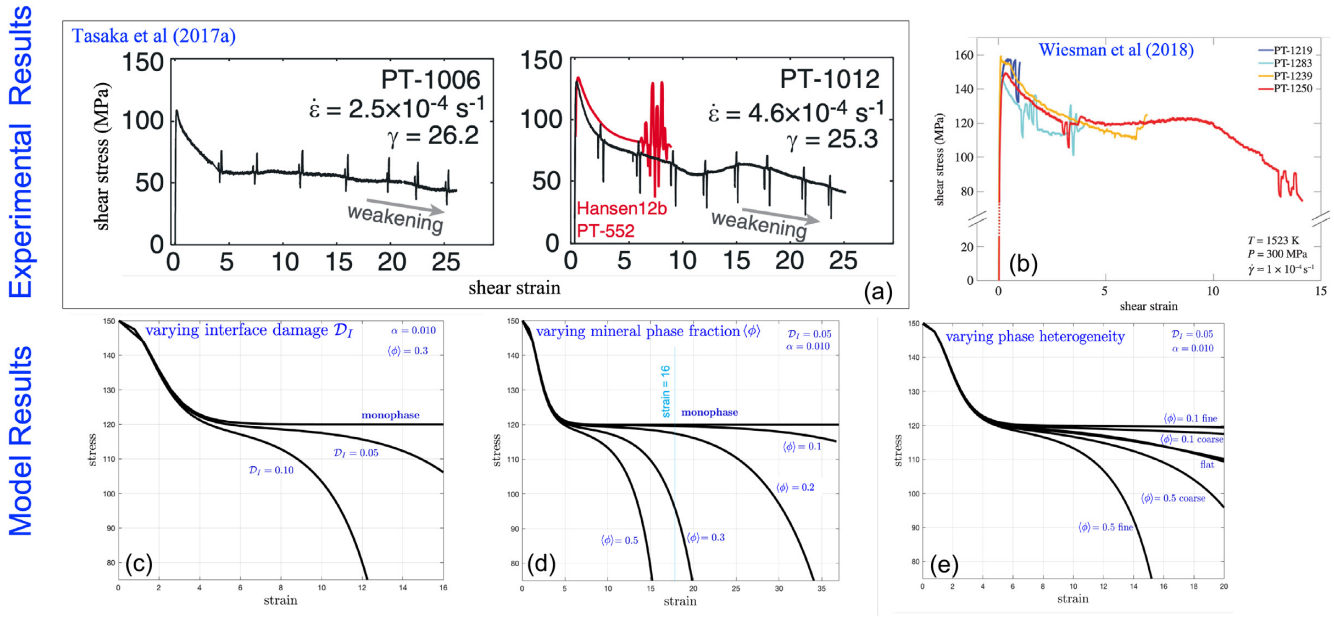

Figure 2. Stress vs strain (equivalent to half the dimensionless time) for no-slip boundaries and polyphase medium for the experiments of Tasaka *et al.* (2017a) (a) and Wiesman *et al.* (2018) (b), compared to the case of numerical model with equivalent boundary conditions and a two-phase medium with Zener pinning and mixing. Fixed parameters for all model cases are $\mathcal{C}_i = 0.2$, $\mathcal{C}_I = 10^{-4}$, $\mathcal{D}_i = 0.185$, but for varying values (indicated in each frame) for interface damage $\mathcal{D}_I$ (c), the mean secondary phase volume fraction $\langle\phi\rangle$ (d), and different degrees of mixing coarseness in the secondary phase heterogeneity, as explained in the text (e). Calculations showing the monophase stress evolution (as indicated) are done by setting the Zener pinning factor to unity but more specifically by setting $\mathfrak{c} = 0$ in eq. (44); see Hansen *et al.* (2012) for the stress evolution in monophase experiments. In the model, the initial grain sizes $R_1 = R_2 = 10$ and $r = 20$.

The experimental conditions on which the dimensionless numbers depend are the sample geometry, temperature, pressure, mixture ratios, initial grain sizes and imposed velocities or stresses. For the sake of clarity, we focus primarily on matching the details of the Wiesman *et al.* (2018) experiments, which indicate the clearest second stress drop, although we keep in mind differences with the experiments of Tasaka *et al.* (2017a, b, 2020). Wiesman *et al.* (2018) deformed polymineralic samples in torsion in which the sample rings were 2.5–3 mm thick; therefore, here, we approximate the half-width as $H = 1.5$ mm. The imposed bulk shear strain rates (total strain rate across the layer) was held to $\dot{e}_0 \approx 10^{-4}\mathrm{s}^{-1}$ and thus we take the top and bottom velocities as $\pm U = \pm 2H\dot{e}_0 = \pm 3 \times 10^{-7}\mathrm{m\,s}^{-1}$. Those deformation experiments were run at a fixed temperature of 1523 K and a confining pressure of 300 MPa. The experimental mixture was 70 per cent olivine by volume and 30 per cent ferropericlase as a secondary phase. [Although ferropericlase is by itself a weaker phase, it was found to have a minor effect on the mixture strength, at least until grain sizes changed; see Wiesman *et al.* 2018, section 4(c).] Given the temperature and shear-rate, using pure olivine rheological properties from Table 1, the stress scale is $\tilde{\tau} \approx 450$ MPa from eq. (60) and the field-boundary grain size scale is $\tilde{R} \approx 10\mu$m from eq. (48). However, since the experiments are not pure olivine, these scales are merely approximate or 'ball-park' estimates. Wiesman *et al.* (2018) adjusted the experimental shear stresses, whose peak is about 150 MPa, for a cylindrical geometry using the corrections from Paterson & Olgaard (2000), and obtained equivalent peak stress of approximately 300 MPa. However, the exact scale for the peak stress is less important than the relative stress drop; thus, for ease of comparison we dimensionalize the peak model stress to match that of the experimental shear stress at 150 MPa (Fig. 2). Moreover, we note that the Tasaka *et al.* (2017a, 2020) torsion experiments were done in a similar apparatus but at lower temperatures of 1473K, the same confining pressure of 300 MPa and over a range of somewhat higher shear strain rates ranging from about $\dot{e}_0 \approx 2 \times 10^{-4}\mathrm{s}^{-1}$ to $5 \times 10^{-4}\mathrm{s}^{-1}$. Moreover, the Tasaka *et al.* (2017a) experiments were done with a 26 per cent by volume mixture of pyroxene in olivine, which is similar to that of Wiesman *et al.* (2018) but with a different secondary phase chemistry. Tasaka *et al.* (2020) used similar experimental conditions but varied the pyroxene fraction from 0.15 to 0.26–0.35. In Wiesman *et al.* (2018), the mean grain size of olivine varied from an initial 3.7 microns to 2.2 μm at a strain of 14, and that of the secondary phase from 3.6 to 1.1 μm, respectively (see their Fig. 3). The average grain sizes reported in Tasaka *et al.* (2017a) decreased from 7.7 to 1.9 μm across a total strain of more than 26, with orthopyroxene grain sizes being consistently lower by a factor of around 1.5–2 (see Tasaka *et al.* 2020, Fig. 7). Despite being at lower temperatures, higher strain rates, and slightly larger grain sizes, the Tasaka *et al.* (2017a) experiments yielded somewhat lower peak stresses than those of Wiesman *et al.* (2018); this might be attributed to possible hardening effects of ferropericlase on olivine [see Wiesman *et al.* 2018, section 4(c)].

Although grain growth laws remain somewhat uncertain (see Karato 1989; Evans *et al.* 2001; Zhang & Karato 2021, and references therein), we assume that the coarsening or healing numbers $\mathcal{C}_i$ and $\mathcal{C}_I$ are somewhat better constrained than the damage numbers $\mathcal{D}_i$ and $\mathcal{D}_I$. Given the properties from Table 1 and the experimental conditions, we fix the healing numbers to $\mathcal{C}_i = 0.2$ and $\mathcal{C}_I \approx 10^{-4}$. With these choices, we now ask what choices of $\mathcal{D}_i$, $\mathcal{D}_I$ and α lead to numerical solutions that best match the experiments. In particular, we seek to recover some of the characteristics of the grain size evolution and the stress–strain measurements from the laboratory experiments.

3.1.1 The first stress drop and two estimates of the grain-boundary damage number $\mathcal{D}_i$

For detailed estimates of the damage numbers $\mathcal{D}_i$ and $\mathcal{D}_I$, we focus on the polyphase deformation experiments of Wiesman *et al.* (2018), for which there are a few important features to consider. First, their experimental mixture initially had reasonably large grains of order a few tens of microns (perhaps up to a maximum size of about 50μm), and as deformation proceeded, grain size reduction was not significant until the mean shear strain $Ut/(2H)$ (which is identical to half the dimensionless time in our model for these fixed-velocity boundary cases) was well in excess of 1. Up to a strain of roughly 4 or 5, the experimental stress dropped from a peak value of 150 to 120 MPa, after which it stabilized to a piezometric equilibrium, until a strain of about 10. This piezometeic plateau can be associated with the monophase piezometric balance for unmixed mineral units, and was also seen in the monophase experiments of Hansen *et al.* (2012). This first stress drop provides a constraint on the grain-boundary damage number $\mathcal{D}_i$.

Specifically, the plateau occurs at a stress of about 80 per cent of the peak value (i.e. 150 MPa at the peak, 120 MPa at the plateau; see Fig. 2b); since the dimensionless model peak stress is 1, the plateau's stress should be 0.8. To estimate the value of $\mathcal{D}_i$ to achieve this stress plateau, we write the steady-state piezometric relation from eq. (58) before mixing and pinning become important (i.e. when $r > R_i$ and $\mathcal{Z}_i \approx 1$):

$$R_i = \left(\frac{\mathcal{C}_i}{p \mathcal{D}_i \tau_i^{n+1}} \right)^{\frac{1}{p+1}} \tag{61}$$

which we can use to eliminate R_i from eq. (55) to obtain

$$\tau_i^n + \tau_i \left(\frac{p \mathcal{D}_i \tau_i^{n+1}}{\mathcal{C}_i} \right)^{\frac{m}{p+1}} - 2\dot{e} = 0 \tag{62}$$

Since $m = 3$ and $p = 2$ for this study, we can infer that

$$\mathcal{D}_i = \frac{\mathcal{C}_i}{p} \frac{2\dot{e} - \tau_i^n}{\tau_i^{n+2}} \tag{63}$$

When this plateau is reached, grains are still initially large and deformation is by dislocation creep, and thus $\dot{e} \approx 1/2$; given other values ($\mathcal{C}_i = 0.2$, $\tau_i = 0.8$, $n = 3.5$ and $p = 2$) we arrive at $\mathcal{D}_i = 0.185$, which requires a grain-boundary damage number of $f_G = 2.7 \times 10^{-5}$ at the given experimental temperatures (again, f_G is inferred to be temperature dependent and increases with decreasing temperature; see Rozel *et al.* 2011; Mulyukova & Bercovici 2017).

The time or strain necessary to reach the stress plateau provides a separate constraint on D_i with which we can check the consistency of the above estimate. Specifically the drop in stress is due to reduction in grain size by grain-boundary damage (i.e. DRX) from $R_i = R_0 > 1$ to $R_i \approx 1$ (i.e. the piezometric plateau is typically near the initial field boundary), assuming again that mixing and interface effects are negligible such that $r > R_i$ and $\mathcal{Z}_i \approx 1$; in this case we can use eq. (58) to write

$$\frac{\mathrm{d}R_i}{\mathrm{d}t} \approx -\mathcal{D}_i \tau_i^{n+1} R_i^2, \tag{64}$$

where we have neglected the coarsening term since $R_i > 1$ during most of the stress drop. We can approximate the time dependence of the stress τ_i, as it drops from the peak value of 1 to the plateau value of $\tau_p = 0.8$ over a time interval Δt by writing $\tau_i \approx 1 - (1 - \tau_p)t/\Delta t$. In this case, the integration of eq. (64) from $t = 0$ to $t = \Delta t$ (or equivalently from $\tau_i = 1$ to τ_p) leads to

$$1 - \frac{1}{R_0} \approx \mathcal{D}_i \frac{\Delta t \left(1 - \tau_p^{n+2}\right)}{(n+2)(1 - \tau_p)}. \tag{65}$$

Assuming $1/R_0 \ll 1$, and using $n = 3.5$ and $\tau_p = 0.8$, we obtain $\mathcal{D}_i \approx 1.56/\Delta t$. In the experiments, the stress drops to the plateau value by a strain of approximately 4, which translates to a dimensionless time interval $\Delta t \approx 8$. Indeed, with $\Delta t = 8.4$ we obtain $\mathcal{D}_i = 0.185$, as estimated independently above. Conversely, the above relation can be used to predict the time to reach the plateau Δt given an estimate of $\mathcal{D}_i$.

3.1.2 The second stress drop and implications for interface damage

After strain exceeds approximately 10–20, mixing between mineral phases at the grain scale becomes significant and is concurrent with grain size reduction, all of which can lead to weakening and a second stress drop (again most clearly seen in the experiments of Wiesman *et al.* 2018). The time (or strain) necessary to reach this second stress drop provides some constraints on how well the phases mix and to what extent the interface between phases is damaged.

In our theoretical model, phase mixing and interface damage depend on several factors, including the interface damage number $\mathcal{D}_I$, the grain-mixing diffusivity α, the mean secondary phase volume fraction

$$\langle \phi \rangle = \tfrac{1}{\Delta A} \iint_{\Delta A} \phi \, \mathrm{d}x \, \mathrm{d}z \tag{66}$$

(where ΔA is the 2-D model domain), and the structure of petrological heterogeneity. The mean phase volume fraction for the secondary phase in the Wiesman *et al.* (2018) experiments was $\langle \phi \rangle = 0.3$; in the experiments of Tasaka *et al.* (2017a) it was 0.26, and for Tasaka *et al.*

(2020) it was varied from 0.15 to 0.26–0.35. In the Earth's upper mantle $\langle\phi\rangle \approx 0.4$ for non-olivine components, mostly pyroxene. The initial structure of the phase heterogeneity is typically randomly dispersed in the experiments and in nature (as represented in Fig. 1), although very coarse and even layered structures with flat interfaces between phases have also been tested by, for example, Linckens *et al.* (2014). For the majority of model calculations, we initiate the heterogeneity with random Fourier series (see Bercovici & Mulyukova 2021, SI, eq. 48) with 8 Fourier or sinusoidal modes in the x direction and 4 in the z direction; alternative coarser and layered heterogeneity are also considered below.

Mixing at the grain-scale is generally observed to be slow (Linckens *et al.* 2014; Cross & Skemer 2017; Tasaka *et al.* 2017a, b, 2020), and is suppressed until the phases are sheared and stretched out enough that large gradients in volume fraction $\nabla\phi$ are achieved, which is also typical of mixing of chemical heterogeneity (see Olson *et al.* 1984a, b; Tackley 2015). We associate this behaviour with low diffusivity such that $\alpha \ll 1$ (see eq. 59). For most cases we assume $\alpha \leq 10^{-2}$, but also explore the effect of its variation below (see Section 3.1.6).

Given a specific α, $\langle\phi\rangle$ and a sufficiently dispersed phase heterogeneity, the timing for the second stress drop provides some constraints on the interface damage number $\mathcal{D}_I$. The delay in stress evolution to the second stress drop requires interface damage to be less effective than that for the grain boundaries, and thus we can infer that $\mathcal{D}_I < \mathcal{D}_i$. For the parameter set given by $\mathcal{C}_i = 0.2$, $\mathcal{C}_I = 10^{-4}$, $\mathcal{D}_i = 0.185$, $\langle\phi\rangle = 0.3$, and $\alpha = 10^{-2}$, then $\mathcal{D}_I = 0.05$ leads to a reasonable match to the stress evolution in the experiments (Fig. 2b). Increasing $\mathcal{D}_I$ by a factor of 2 to $\mathcal{D}_I = 0.1$ almost halves the time to reach the 2nd stress drop. However, we fix this parameter to $\mathcal{D}_I = 0.05$ in order to explore the sensitivity of other parameters and conditions.

3.1.3 Influence of phase fraction on stress evolution

As investigated experimentally by Tasaka *et al.* (2020), the amount of secondary phase has a significant influence on grain size evolution and mode of deformation. Our model results also imply that the amount of secondary phase has a profound influence on the occurrence of the second (although not the first) stress drop. Obviously for $\langle\phi\rangle = 0$ the system is monophase for which there is no second stress drop. A second stress drop occurs eventually even for small $\langle\phi\rangle$, but unless $\langle\phi\rangle \geq 0.3$ it would be difficult to detect within the experimental strains of less than 15 (Fig. 2d). The fastest stress drop occurs, as expected, for an even mixture of phases with $\langle\phi\rangle = 0.5$. However the timing for the stress drop only becomes increasingly sensitive to $\langle\phi\rangle$ when it is <0.3. For example, the strain (or half the dimensionless time) at which the stress goes from the plateau value of $\tau = 120$ to $\tau = 110$ MPa, occurs at a strain of 12 for $\langle\phi\rangle = 0.5$, at 15 for $\langle\phi\rangle = 0.3$, but then at 25 for $\langle\phi\rangle = 0.2$ and then greater than 40 for $\langle\phi\rangle = 0.1$.

Our numerical simulations show that for $\langle\phi\rangle > 0.3$, the weakened, mixed zones in between monophase units are spatially frequent enough that, at high strains, they interconnect sufficiently to weaken the entire layer. But for smaller $\langle\phi\rangle < 0.2$, the mixed zones stay isolated and disconnected, and the stiffer, large-grain monophase regions dominated the layer's strength. However, it should be noted that while Tasaka *et al.* (2020) explored the effect of phase fraction in polyminerallic torsional experiments, they did not document significant second stress drops, and observed only a gradual decline in stress at high strains. However, they noted that for pyroxene fractions of $\langle\phi\rangle < 0.15$ the phase mixing was insignificant and the deformation mechanism stayed close to that of the monophase case, with dislocation creep dominant flow. For $\langle\phi\rangle > 0.26$ at large strains >10, grain mixing became pervasive and was concurrent with reduced olivine grain sizes; the deformation mechanism also changed notably away from a dislocation creep, power-law stress–strain rate relation (i.e. the effective power law exponent shifted from $n \approx 3$ to $n \approx 2$, implying either an increased role of diffusion creep or, as those authors contend, the onset of dislocation accommodated grain-boundary sliding). Other polyphase experiments, in which one phase is intrinsically weaker than the other, also show that the samples remain strong for phase fractions less than approximately 20–30 per cent (e.g. Handy 1994).

3.1.4 Influence of phase dispersal on stress evolution

The effect of mean phase fraction $\langle\phi\rangle$ also depends on the spatial distribution of the phase heterogeneity, what we refer to as *phase dispersal* (i.e. the size and distribution of monophase units). The cases for which mixing, grain size reduction and weakening leads to a second stress drop were (as mentioned above) for initial heterogeneity in ϕ with 8 Fourier modes in x and 4 in z, and thus relatively finer heterogeneity and greater phase dispersal. Simulations with coarser heterogeneity or less phase dispersal (with 4 modes in x and 2 in z) were also calculated, as were ones with horizontally flat, uniform initial states with 0 modes in x and 2 in z. (These different degrees of phase dispersal are also used below in Section 3.1.6 and illustrated in Fig. 6.) Our calculations show that the phase dispersal modulates the effect of the secondary phase, as might be expected (Fig. 2e). Specifically, for horizontally flat structures in ϕ, the interface area, and hence regions of mixing, grain size reduction and weakening, are the same no matter the value of $\langle\phi\rangle$; this interface area is (in 2-D) just twice the length of the domain L (the factor of 2 occurs because there are 2 Fourier modes in z, leading to one long stripe of secondary phase, whose width is proportional to $\langle\phi\rangle$). Indeed, in the flat heterogeneity case, the stress evolution is essentially unaffected by the value of $\langle\phi\rangle$ and the second stress drop (from 120 to 110 MPa) occurs at around a strain of 19. For the coarse heterogeneity (4 Fourier modes in x, 2 in z), the second stress drop happens sooner for $\langle\phi\rangle = 0.5$ and later for $\langle\phi\rangle = 0.1$, as expected, since there will be more interconnected weak zones with more secondary phase and mixing regions, and fewer such zones with vanishingly small amounts of secondary phase. For the finest heterogeneity and greatest phase dispersal (8 Fourier modes in x, 4 in z), this stress drop is faster yet for $\langle\phi\rangle = 0.5$, and slower yet for $\langle\phi\rangle = 0.1$, since there is an even greater population of weak zones, but they are only readily connected for significant amounts of secondary phase, and too remote to connect if there is too little secondary phase (see also Handy 1994, fig. 10).

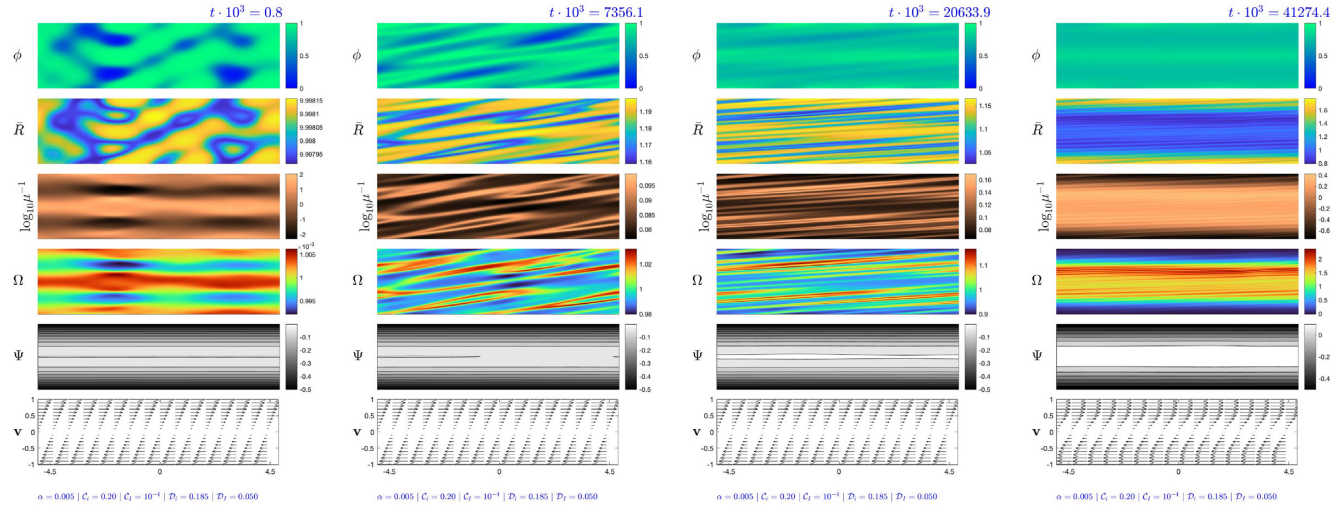

Figure 3. Fields (as indicated) versus time for the case of no-slip boundaries and polyphase medium with Zener pinning and mixing. Parameters are that $\alpha = 0.005, \mathcal{C}_i = 0.2, \mathcal{C}_I = 10^{-4}, \mathcal{D}_i = 0.185, \mathcal{D}_I = 0.05$ with initial grain sizes $R_1 = R_2 = 10$ and $r = 20$, and a 70–30 mix of phases. Dimensionless time is indicated on the upper right above each column of field snap-shots. Strain is equal to half the dimensionless time.

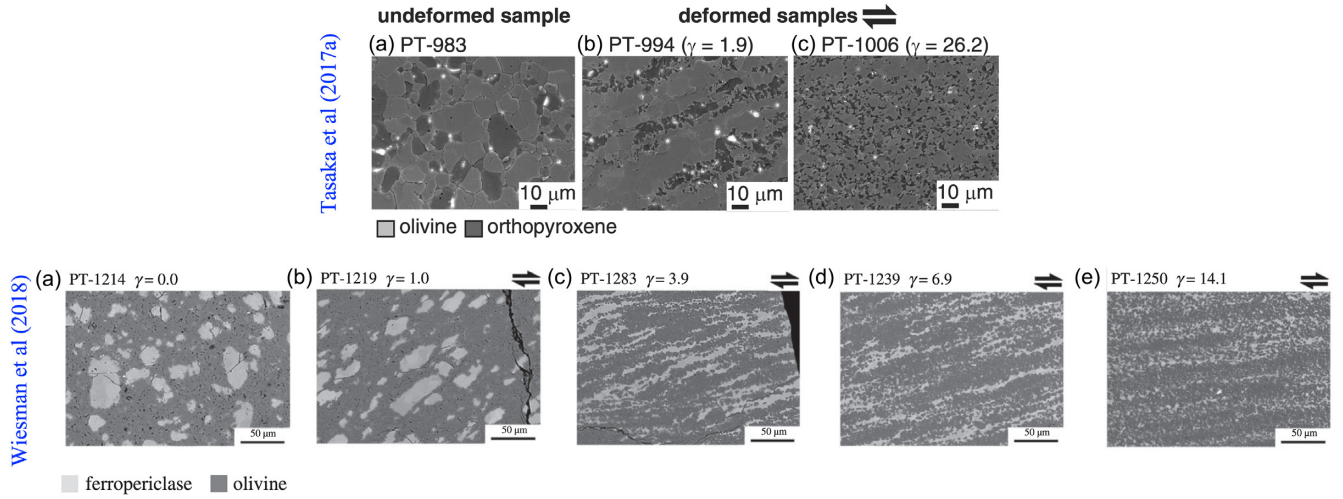

Figure 4. Petrographs showing the microstructural development with increasing strain (γ) for the polyphase experiments of Tasaka *et al.* (2017a) (top row) and Wiesman *et al.* (2018) (bottom row). Figures adapted from those papers.

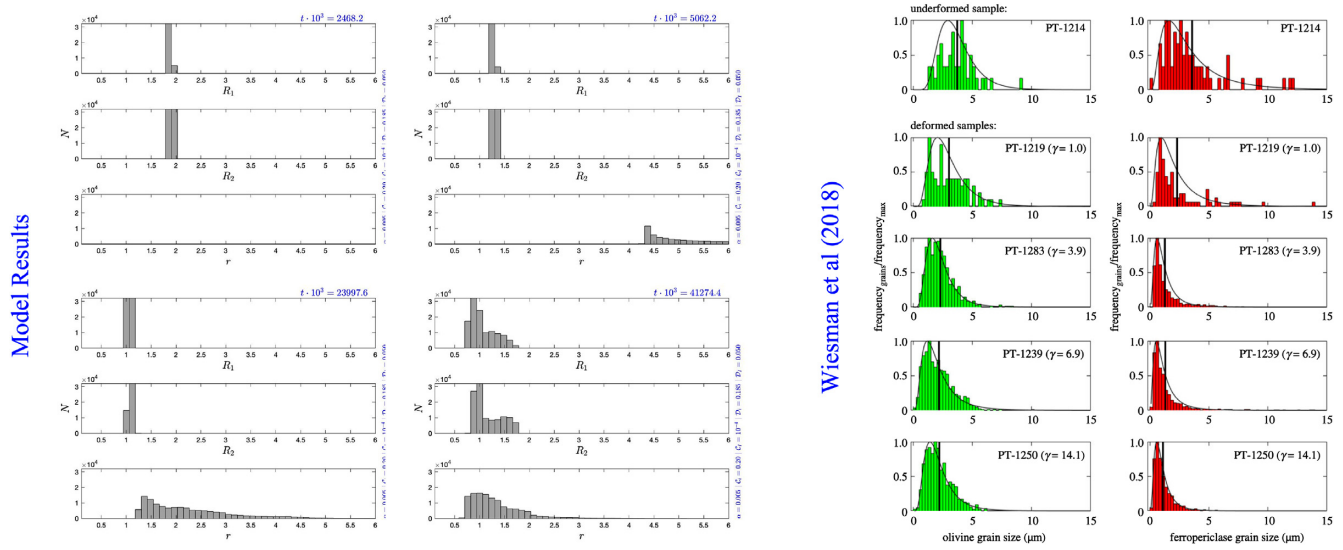

Figure 5. Model results (left-hand panel) for the distribution of grain sizes R_i and interface roughness r at four dimensionless times for the fixed-velocity boundaries as in Fig. 3, and grain size distributions from the experiments of Wiesman *et al.* (2018) (right-hand panel). Note that the model distributions are taken over the whole spatial domain, while those for the experiments were taken over an approximately 200 μm wide domain near the maximally deformed regions within a sample that is approximately 2000 μm wide. Also note, for fixed velocity cases, the model dimensionless time is equivalent to twice the strain.

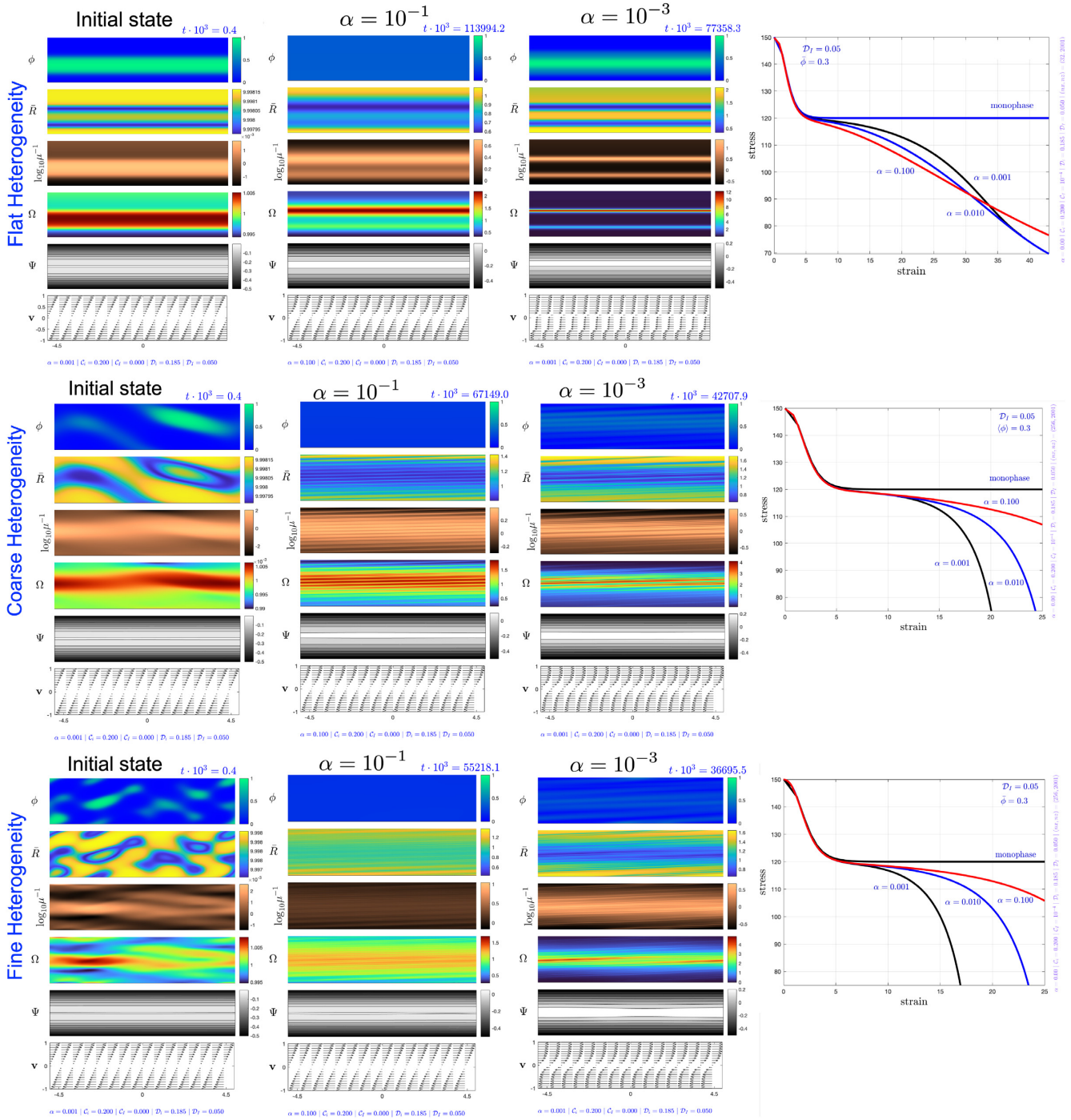

Figure 6. Model results for the fixed-velocity boundaries showing field quantities (as in Fig. 3), and stress versus strain (as in Fig. 2) for a sampling of the grain-mixing diffusion factor α from 10^{-3} to 10^{-1}, and for three levels of phase dispersal, that is from horizontally flat interfaces between mineral phases (top row), to a coarse structure (middle row), to a finer structure (bottom row), all of whose Fourier modes are discussed in the text. Other than variations in α as indicated, other dimensionless numbers are fixed to $\mathcal{C}_i = 0.2$, $\mathcal{C}_I = 10^{-4}$, $\mathcal{D}_i = 0.185$, $\langle\phi\rangle = 0.3$ and $\mathcal{D}_I = 0.05$.

3.1.5 Evolution of 2-D structure and grain size distribution

For cases in which the choice of dimensionless parameters allows both first and second stress drops corresponding to the experiments, we track the evolution of the various 2-D fields in volume fraction ϕ, mean grain size $\bar{R}$, viscosity μ (or compliance μ^{-1}), as well as those quantifying deformation and flow, such as vorticity Ω, stream-lines or contours in Ψ, and the velocity field $\mathbf{v}$ (Fig. 3). These cases demonstrate how grain size and hence viscosity reduction is concentrated on the interface between monophase units, where mixing occurs, and these weak, rapidly deforming zones are stretched out laterally while weakening further, until they are interconnect and cause the whole layer to weaken.

By strains of 10, grain size reduction concurrent with phase mixing is evident, and by strains of 20 mixing is pervasive enough to erase most of the signature of compositional heterogeneity, as also evident in the experiments (Fig. 4).

The evolution of the the distributions in grain sizes R_i and interface roughness r also reveals the stages of mixing and damage corresponding to the two stress drops (Fig. 5). Initially, the grain sizes R_1 and R_2 reach their monophase piezometric values relatively quickly during the first stress drop, and remain relatively unaffected by mixing (during the stress plateau) until the interface roughness r shrinks enough to drive the grains sizes—via the action of Zener pinning—below the field boundary, to mylonitic sizes, initiating the second stress drop. The experimental grain size distributions are qualitatively comparable to the models with some notable exceptions. As with the model calculations, the experimental distributions show a progression of moderately decreasing modal (peak) grain sizes. The model calculations, however, initiate with a mono-modal initial state and the distribution spreads out even as the modal grain size reduces. The experiments start off with a wider distribution, which narrows as the modal size reduces. Moreover, while the reduction in grain size differs little between phases in the model, it is somewhat more notable in the experiments, wherein the secondary phase grain sizes reduce more than those in the primary phase; this trend is seen in both the experiments of Wiesman *et al.* (2018; shown in Fig. 5) as well as those of Tasaka *et al.* (2017b). However, it should be noted that the model distribution is sampled over the whole domain, while that of the experiments focusses on the zone of localized deformation; thus larger grain sizes in the less localized zones are also sampled in the model cases.

3.1.6 Influence of grain-scale diffusive mixing

Mixing at the grain scale remains the least understood process in this model, and whether it is due to chemical or mechanical migration of matter along grain boundaries is uncertain. Our treatment of it as a diffusive process is a mathematical model, designed to allow for stress-driven anisotropic diffusivity that satisfies mass conservation and the second law of thermodynamics (by disallowing any negative diffusion). Overall, compositional heterogeneity in our model evolves due to advection and stirring through macroscopic flow and diffusive grain scale mixing; both effects interact with each other and influence weakening and shear localization.

Heterogeneities in a non-deforming medium, or a deforming medium in which the spatial structure of heterogeneity is parallel to the direction of shear flow (e.g. a horizontal flat structure subjected to purely horizontal flow, such that advection has no effect) will diffusively mix in the direction of the initial compositional gradients (i.e. $\nabla\phi$), which smooth out with time. More rapid diffusive mixing between phases occurs with higher intrinsic diffusivity (represented by α in our model), which leads to wider mixed regions in which Zener pinning occurs; this in turn inhibits grain growth and, if the medium is deforming, facilitates grain damage that leads to more pervasive grain size reduction, weakening and a drop in stress.

However, if the medium is deforming and heterogenous in all directions (i.e. not just a flat heterogeneity), then the compositional anomalies can become sheared and distorted (see Fig. 3), thereby amplifying the gradients that drive diffusive fluxes. If the intrinsic diffusivity α is low, heterogeneity can be extensively sheared leading to extremely sharp gradients $\nabla\phi$, which then drive large diffusive fluxes despite the low diffusivity (see Olson *et al.* 1984b). Moreover, the deformational work associated with mechanical grain-scale mixing, which contributes to interface damage (see eq. 57) can be large even for cases of low diffusivity (e.g. small α). In the end, sharper gradients in phase fraction ϕ lead to narrower mixed zones in which Zener pinning and interface damage are focussed, and hence where grain size reduction and weakening is enhanced. As deformation is then localized on the weak zones their deformational work is likewise amplified, leading to more damage and weakening, and so on, in the classical shear-localizing feedback.

Thus while more rapid diffusion would facilitate wide-scale mixing and Zener pinning, slower diffusion promotes weaker localized bands and thus stress reduction. These effects can be separated and illustrated by considering heterogeneity with increasing *phase dispersal*. In particular, flat compositional structures (uniform in x) with weak phase dispersal, suppress the shearing and stretching of heterogeneity, and the effect of diffusion without the influence of deformation dominates (Fig. 6 top panel, as indicated). In this case, stress initially drops fastest for the largest diffusivity α (Fig. 6 top, right frame, red curve), since the more rapid mixing allows wide-scale grain size reduction and weakening, especially when there can be no more than two localized weak zones. However, even in this case, the focussed weakening and damage for the cases with smaller α allow the stress drop to catch up and surpass that of the large α case at high strains (Fig. 6 top panel, right frame, black and blue curves).

But, for cases in which compositional structure is not flat, with increasing phase dispersal that is either coarse or fine in both the x- and z-directions (Fig. 6 middle and bottom panels, as indicated), shearing and stretching enhance heterogeneity and lead to more focussed zones of mixing and deformation. These effects allow the cases with smallest diffusivity α to weaken the fastest and undergo the most rapid second stress drops, which is the reverse for the flat-heterogeneity case (at least up to moderate strains).

The effect of diffusive mixing can possibly be used to explain some variation between experiments, at least for those with the same composition. Specifically, Tasaka *et al.* (2017a) found a moderate second stress drop at high strains for applied larger strain rates, but less evidence of weakening for smaller strain rates (see Fig. 2a). Since the inverse of strain rate $\dot{e}$ sets the time-scale for the model calculations, the higher strain rate cases would be associated with the smaller α (i.e. α represents diffusion rate normalized by strain rate) and hence more profound weakening, according to the model. However, the explanation is more difficult to apply in comparing the experiments of Tasaka *et al.* (2017a) to those of Wiesman *et al.* (2018) (see Fig. 2b). The latter study was done at higher temperature and lower strain rates, which in principle should lead to large α, but nonetheless yielded a much more notable stress drop than the study of Tasaka *et al.* (2017a). Whether this disparity can be reconciled with the diffusion model is difficult to say at this point, given the sparse experimental coverage, with only two experiments at high strain with the same chemistry (Tasaka *et al.* 2017a), and one with a different chemistry (Wiesman *et al.* 2018).

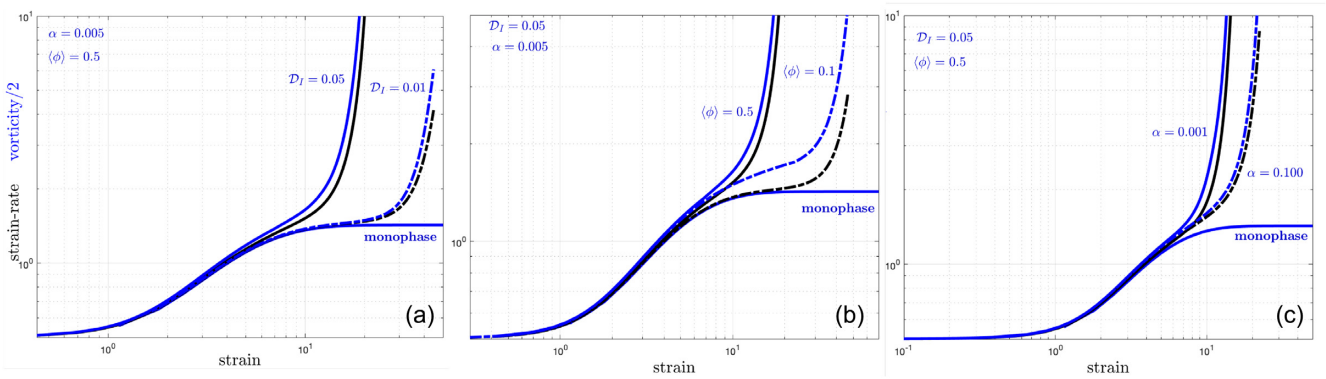

Figure 7. Mean strain rate across the layer $\frac{1}{2}(\bar{u}_{top} - \bar{u}_{bot})/(z_{top} - z_{bot}) = \Delta\bar{u}/4$ (where $u = \Omega_0 z - \partial\psi/\partial z$, as in (49); and $\bar{u} = (2L)^{-1}\int_{-L}^{+L} u\mathrm{d}x$ and $z_{\rm top} = -z_{bot} = 1$) versus strain ($\int_0^t \Delta\bar{u}/4\mathrm{d}t$), for the case with fixed-stress boundaries. Half the maximum vorticity $\frac{1}{2}\max(\Omega)$ is also shown as a proxy for local shear rate. Different cases with varying parameters that control interphase mixing and interface damage are shown, specifically for different $\mathcal{D}_I$ (a), different $\langle\phi\rangle$ (b) and different α (c). The monophase curves are calculated by setting $\mathfrak{c} = 0$ in eq. (44) and the initial $R_1 = R_2$. For all cases, $\mathcal{C}_i = 0.2$, $\mathcal{D}_i = 0.185$, $\mathcal{C}_I = 10^{-4}$, and the initial heterogeneity uses 8 random Fourier modes in x and 4 in z, as shown in Fig. 8.

Moreover, while those sets of experiments were done in the same laboratory apparatus, their comparison is not straight forward. In particular, while the experiments of Tasaka *et al.* (2017a) were at a lower temperature, higher strain rate and with a stronger secondary phase than those of Wiesman *et al.* (2018), the former's peak stresses were lower than the latter's. Wiesman *et al.* (2018) attributed their higher intrinsic sample strength to either buffering at low silica activity due to the introduction of ferropericlase (MgO), or inhibition of disGBS at phase-boundaries by MgO. Either way, the unexpected hardening possibly due to the different silica-free chemistry of the secondary phase might also play a role in the grain-mixing diffusivity due to either chemical (Tasaka *et al.* 2017b) or mechanical (Bercovici & Skemer 2017) processes. For example, if weakening due to phase-boundary sliding, as inferred in olivine–clinopyroxene composites (Zhao *et al.* 2019), is more effective in olivine–orthopyroxene than in olivine–ferropericlase, it could lead to faster mixing diffusivity in the former ol-opx composites, provided the grain-mixing occurs mechanically as per Bercovici & Skemer (2017). In the end, resolving the mechanisms for grain-scale mixing calls for a wider range of experiments with varying strain rates and/or temperatures for given compositions, in conjunction with model refinement with which to test theory against experiments.

3.2 Fixed stress boundaries

Deformation with fixed stress boundary conditions is significantly different than that for fixed velocity conditions. With fixed velocity boundaries, both the stress $2\mu\dot{e}$ and energy input $2\mu\dot{e}^2$ diminish as viscosity decreases. But for fixed stress boundaries, the strain rate $\tau/(2\mu)$ and energy input $\tau^2/(2\mu)$ increase as viscosity decreases. Thus, shear localization and/or weakening is manifest as a stress drop in the former (as discussed above), but as a strain rate jump in the latter.

However, because of the technical challenges of keeping applied torsional stress constant, deformation experiments with fixed stress boundaries are rarer than those with fixed velocity boundaries. Although some experiments with fixed stress in monophase samples were done by Hansen *et al.* (2012), those in polyphase media have (to our knowledge and also that of L. Hansen personal communication) not been performed. Regardless, we attempt to simulate potential experiments with our model, using the same parameters gleaned from the comparison to the fixed-velocity experiments.

3.2.1 Strain rate evolution

For the model monophase case, strain rate increases to a steady state plateau (in contrast to the fixed velocity where stress drops to a plateau). This plateau strain rate can be estimated using eq. (62) to write

$$\dot{e} = \frac{1}{2}\left(\tau_i^n + \tau_i\left(\frac{p\mathcal{D}_i\tau_i^{n+1}}{\mathcal{C}_i}\right)^{\frac{m}{p+1}}\right) \tag{67}$$

which for a dimensionless imposed stress of $\tau_i \approx 1$, and other parameters inferred previously (i.e. from Table 1 and from the fixed velocity experiments discussed in the previous section) namely $\mathcal{C}_i = 0.2$, $\mathcal{D}_i = 0.185$, $n = 3.5$, $m = 3$, $p = 2$, we arrive at $\dot{e} = 1.425$ (as verified in the numerical calculations: see Fig. 7, monophase curves), which is nearly three times larger than that for the starting condition of pure dislocation creep for which $\dot{e} = 1/2$.

For the polyphase cases, this first stress plateau is also reached identically to the monophase ones, but then the strain rate departs from the plateau and increases rapidly; for these cases, the strain rate is not uniform and thus the mean strain rate and local maximum shear rate (a proxy for which is half the maximum vorticity) can differ. The strain at which the strain rate departs from the monophase plateau is again governed by the influence of the secondary phase on grain size evolution through interface damage and mixing. For small interface damage

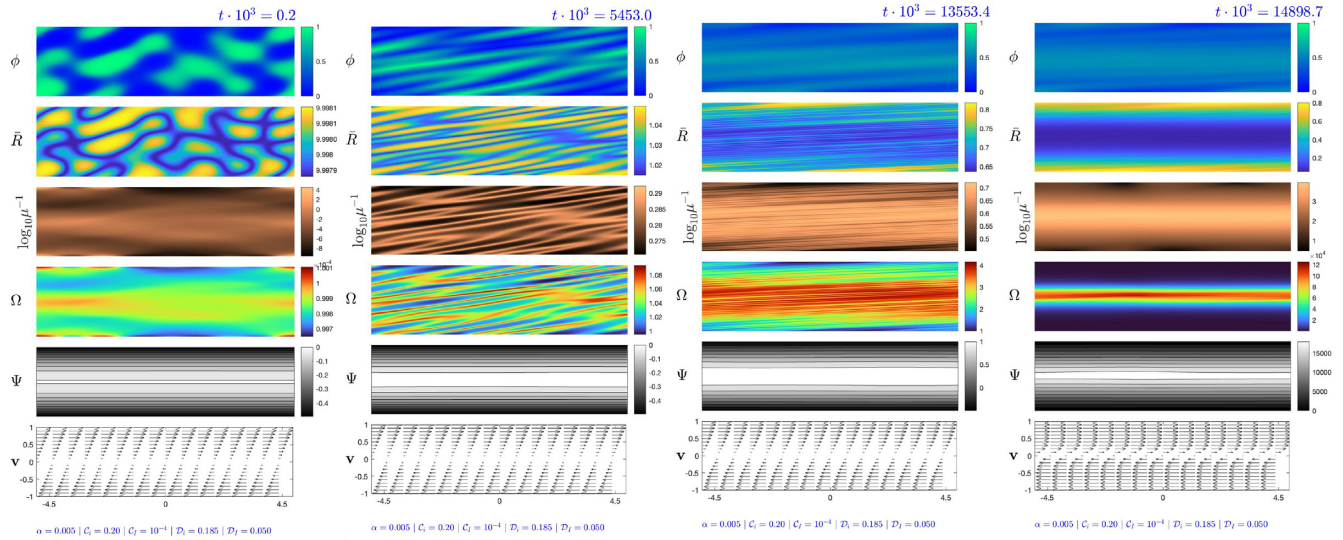

Figure 8. Fields versus time for the case of fixed stress boundaries and polyphase medium with Zener pinning and mixing. Parameters are $\alpha = 0.005$, $\mathcal{C}_i = 0.2$, $\mathcal{C}_I = 10^{-4}$, $\mathcal{D}_i = 0.185$, $\mathcal{D}_I = 0.05$ with initial grain sizes $R_1 = R_2 = 10$ and $r = 20$.

numbers, for example $\mathcal{D}_I = 0.01$, the strain rate remains on the monophase plateau to strains of order 20–30 before departing to higher values. For larger interface damage numbers, such as $\mathcal{D}_I = 0.05$, the strain rate departs for higher values soon after bending towards the monophase plateau at strains <10 (see Fig. 7a).

As with the constant velocity boundary cases, the bulk phase mixture fraction $\langle\phi\rangle$ (see eq. 66) also plays a role in the weakening and localization, which causes the strain rate to depart from the mono-phase plateau (Fig. 7b). Specifically, weakening and localization occur soonest for an even mixture of $\langle\phi\rangle = 1/2$, and later for smaller $\langle\phi\rangle$; the strains at which departure from the monophase plateau occurs is similar to that for the constant velocity case (i.e. at which the second stress drop occurs).

The effect of grain-mixing diffusivity α also plays a similar role as in the constant velocity cases. Again, provided distributed phase heterogeneity, smaller diffusivity α leads to more rapid weakening and localization associated with phase mixing and grain damage (Fig. 7c).

3.2.2 Heterogeneity and grain size evolution

As with the fixed-velocity simulations, when the mixture is sheared to strain of about 5–10, the grain sizes reduce to their single-phase piezometric balance at a value of around $R_i \approx 1$ (see Fig. 8 at time $t \approx 5$). (Note since the strain rates are higher for the constant stress case, strain is larger than half the dimensionless time, and even much larger when strain rate increases rapidly.) Interface damage and grain-mixing allows the interface roughness r to reduce to small sizes at strains of around 5–10, which then triggers reduction of the minimum grain size to significantly less than 1 (see Fig. 8 for frames with $t > 10$), prompting the final weakening and localization and jump in strain rates.

The evolution of the distribution in both grain sizes and interface roughness are (as with the fixed velocity cases) informative about the sequences leading the final weakening (Fig. 9). Initially the grain sizes R_i rapidly reduce to their first piezometric state while the interface roughness r lags behind. Eventually the roughness reduces to $r \leq R_i$, at which point Zener pinning enhances grain damage and helps drive the grains to much smaller sizes than unity (Fig. 9 final times), associated with the rapid weakening and localization (Fig. 7). Note again that, while localization happens sooner in time t, since the strain rate is always increasing, the strain climbs faster than does time (unlike the fixed velocity case); thus the abrupt localization happens at around a strain of 10, similarly to the fixed velocity cases.

3.2.3 Note on fixed-stress, but monophase experiments

Hansen *et al.* (2012) performed both fixed velocity and fixed stress torsional experiments on monophase olivine samples. Their fixed stress conditions were approximately maintained by having a feedback to their continuous stress measurements, tuning the deformation rate to keep stress within a given range. While their fixed velocity experiments induced the expected stress drop to a piezometric steady state (discussed above), the fixed stress experiments led to somewhat unexpected results in the evolution of strain rate. In principle, if the rheological behaviour followed a composite creep rheology as in eq. (33), the strain rate would adjust to a steady state piezometric level, as discussed above (see Fig. 7, monophase curves). However, while the experiments of Hansen *et al.* (2012) suggest some levelling off of strain rate after an initial increase, it undergoes a secondary increase at high strains, which those authors suggest is due to grain size sensitive rheological behaviour during dislocation accommodated grain-boundary sliding (disGBS). A secondary increase in strain rate is only seen in our model when a secondary phase is present (Fig. 7, polyphase curves). In a single-phase system with only one evolution equation for grain size R, it is mathematically impossible to get an unstable oscillation as seen in the experiments, even if one of the rheological regimes included a creep law

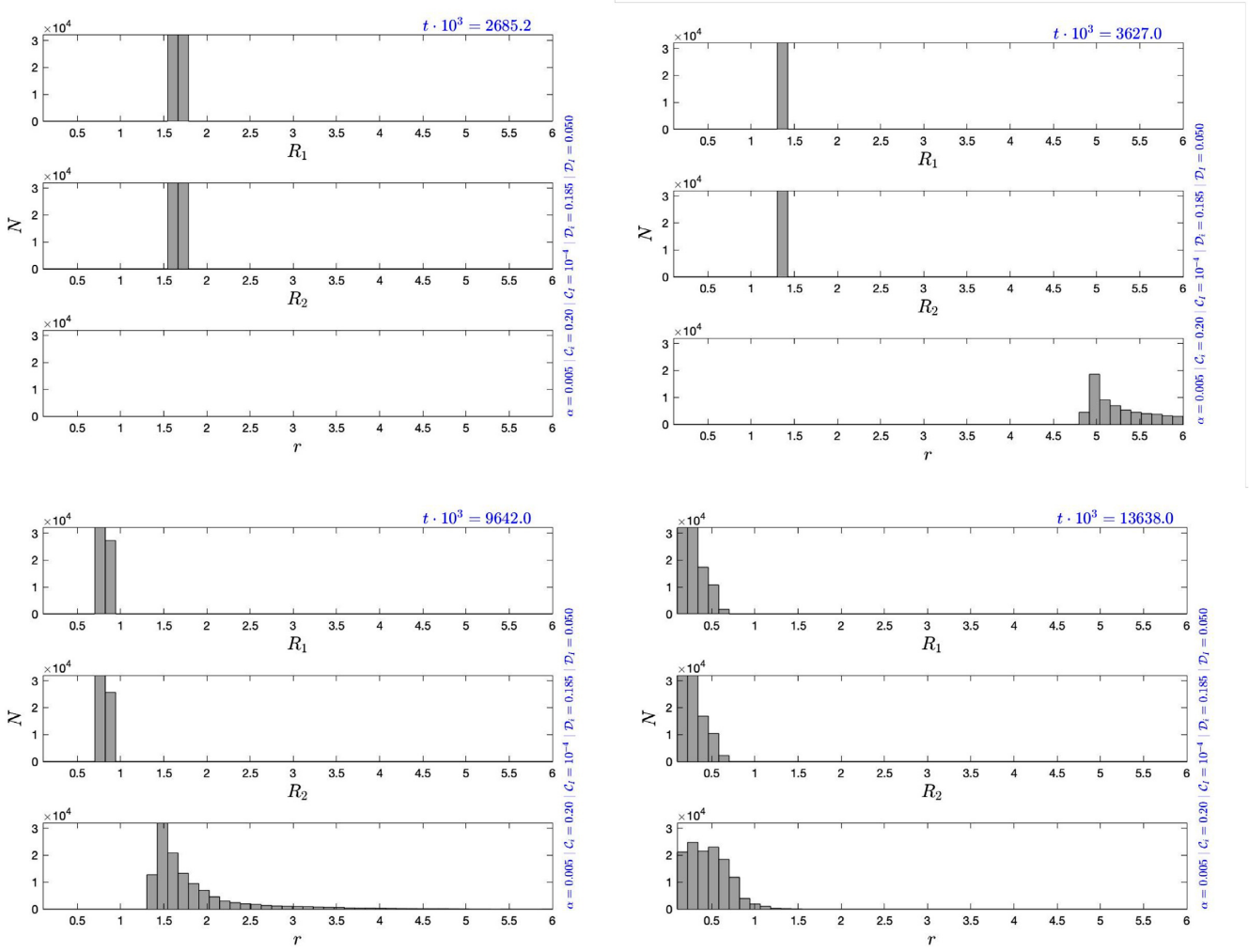

Figure 9. Distribution of grain sizes and interface roughness versus time for constant stress boundaries as in the case of Fig. 8. These are distributions over the whole domain.

for disGBS (i.e. a composite law for diffusion, dislocation and disGBS creep). Specifically, an oscillation requires at least two time-dependent variables associated with two prognostic evolution equations. Conceivably the oscillation arises from other effects not included in a monophase grain-damage model, such as non-steady-state (transient) creep or dislocation dynamics (Mulyukova & Bercovici 2018, 2022), or because of impurities that amount to a secondary phase.

Until more experiments can be run, including in polyphase systems, this issue remains enigmatic. However, this again calls for more systematic experiments, with which to test theory and elucidate the physics of grain-mixing.

4 DISCUSSION AND CONCLUSIONS

In this paper, we have endeavoured to develop a numerical model that couples two-phase grain damage and phase mixing through a 2-D flow model that can be compared to torsional deformation experiments of polymineralic mantle materials and their analogues. By linking theory and experiments we seek to deepen the physical framework for understanding the formation of upper-mantle mylonites, which are likely the key to a theory for the generation of plate tectonics. In particular, our goal is to provide reasonably detailed quantitative comparisons between model and experiments to help elucidate the physics, test the theory and its limitations and potentially guide future experiments for further tests.

Much of our comparison to experiments focussed on samples in simple shear with top and bottom boundaries driven at constant velocity, which is the most commonly used boundary condition in torsional deformation experiments. For constant velocity boundary experiments, the starting grain sizes are relatively large and the initial peak stress is dictated by dislocation creep rheology at the predominant strain rate. The stress then drops towards a piezometric steady state or plateau by a strain of around 4 or 5, as is also typical of monophase experiments and models. For monophase experiments, this plateau persists to large strains for the duration of the experiment. However, for

polyphase experiments, the stress can undergo a second large drop at much larger strains (of order 10 or larger), and which is associated with grain-mixing, grain size reduction into grain size sensitive creep and subsequent weakening.

Model calculations for polyphase media with grain mixing and damage capture the experimental behaviour of the two stress drops, which provides useful constraints on the damage processes in the model. Specifically, the first stress drop to the equivalent monophase plateau constrains the damage directly to grains, in particular the amount of deformational work going towards making new grain-boundary surface energy, nominally through dynamical recrystallization; this damage process is no different than that in the monophase damage model (e.g. Ricard & Bercovici 2009; Austin & Evans 2007; Rozel *et al.* 2011). The second stress drop is unique to the two-phase system and occurs when damage to the interface between phases (rate of deformational work going to interface surface energy) is moderately slower or less efficient than damage to the grain boundaries. It is worth noting that grain and interface damage (i.e. generating new grain boundaries and new interface area, respectively) occur through different microphysical processes; the former is accommodated largely by dislocation dynamics, and the latter by phase stirring through deformation, along with mechanical or chemical phase mixing. Moreover, phase-boundary sliding (Zhao *et al.* 2019) might also induce different deformation behaviour at the interface between phases; specifically, its inferred weakening effect would potentially lessen interface damage. It is therefore not surprising that the grain-boundary and interface (phase-boundary) damage numbers are different. The timing or strain for the second stress drop provides important constraints on the interface damage process.

The second stress drop, however, is also influenced by other factors. The bulk phase fraction (i.e. the volume fraction of the secondary phase) influences the timing and magnitude of the second stress drop, wherein an even mixture yields the most profound drop, and as the volume fraction goes to zero (the monophase limit) the second stress drop vanishes, as expected. The structure of compositional or phase heterogeneity also affects the second stress drop, that is whether the phases are initially dispersed into more or less random 2-D structures, or aligned into flat layers parallel to the direction of flow. Flat structures tend to suppress the effect of the secondary phase volume fraction, since the zones of mixing between phases are simply the length of the domain no matter the volume fraction. As the phase heterogeneity becomes more dispersed and refined (with smaller wavelength features), the influence of volume fraction becomes more profound.

The second stress drop is also affected by the grain-mixing diffusivity, which nominally models how stress drives phase mixing at the grain-scale through mechanical or chemical transport along grain-boundaries. The physics of this mixing remains an open question in the topic of polyminerallic deformation. Larger grain-mixing diffusivity promotes a faster stress drop if simple diffusion is dominant, as in a system with flat phase heterogeneity. But when the heterogeneity is dispersed and refined, smaller grain-mixing diffusivity leads to a more rapid stress drop; this occurs because distorted heterogeneities in shear sharpen when diffusivity is low, and this leads to narrow and rapidly deforming mixed regions that sustain intense grain reduction, localization and weakening. This effect can be used to explain variation in laboratory results for experiments with fixed composition; it is less obvious how this connects experiments with different chemical composition.

For simplicity, we have assumed that both mineral phases in our model have similar rheological behaviour. This approximation is reasonable for the peridotite mixtures of olivine and pyroxene (Tasaka *et al.* 2017a, b); it also appears reasonable for the olivine–ferropericlase mixtures, which (despite ferropericlase being intrinsically weaker) exhibit similar strength to that of pure olivine (Wiesman *et al.* 2018). However, recent work of Cross *et al.* (2020) showed that grain mixing is suppressed in phases with large contrasts in viscosities, presumably because deformation is concentrated in the weak phase, thus limiting the distortion and stretching of polyphase units. The effect of high viscosity contrast between phases can be incorporated into the model, but we defer this to future possible studies.

Experiments with constant stress boundary conditions are technically difficult and thus rare, and therefore only done (so far) with monophase systems. However, using constraints on the physics and physical parameters gleaned from the constant velocity cases, we modelled constant-stress boundary experiments with an eye to guiding future possible experiments. For this system, strain rate rather than stress evolves, and it increases during weakening and localization. For a monophase medium, there is theoretically a single strain rate increase to a piezometric steady state plateau. But for the polyphase model, the strain rate undergoes a second abrupt increase, the timing for which is again controlled by interface damage and parameters governing mixture ratios and grain mixing.

Much of the same physical interpretations on the physics and causes for the second abrupt change (in stress or strain rate) can be applied to both the constant velocity and constant stress systems. The timing of the second changes is controlled primarily by the interface damage that roughens the interphase boundary. However, the bulk phase fraction, the structure of the compositional heterogeneity and the grain-mixing diffusivity also influence the second abrupt changes in both systems, although these quantities are less likely to vary in the upper mantle. However, the physics of diffusive grain-mixing warrants further investigation.

Lastly, the evolution of the microstructure, both the deformation of phase heterogeneity but also the grain sizes in both phases and the interface roughness (or mixing surface) between phases are matched reasonably well between model and experiments. The intense shearing of heterogeneity is well correlated with grain-mixing and grain size reduction at high strains, as observed in the experiments. But the delayed second stress drop (or second strain rate increase) is also measured in the model by the lag in the decrease in interface roughness distribution relative to the grain size distributions in both phases; that is the grains recrystallize relatively rapidly to sizes given by a monophase piezometric equilibrium, but the interface becomes rougher more slowly and eventually drags the grain sizes—through the action of Zener pinning—to much smaller values, and into the diffusion creep regime, where localization feedbacks can proceed.

In the end, our study provides a framework for comparison, testing and calibrating theory with experiments and thus is a means for better scaling the microphysics up to geodynamic and planetary scales. However, our analysis also opens up many questions that suggest and warrant further systematic joint experimental and modelling studies.

DATA/CODE AVAILABILITY

All original results are numerical. Fortran codes for the numerical models are available on request.

ACKNOWLEDGMENTS

This work was supported the collaborative NSF grants EAR-1853184 (for EM and DB) and EAR-1853155 (for PS).

REFERENCES

Austin, N. & Evans, B., 2007. Paleowattmeters: a scaling relation for dynamically recrystallized grain size, *Geology,* **35,** 343–346.

Bercovici, D., 1993. A simple model of plate generation from mantle flow, *Geophys. J. Int.,* **114,** 635–650.

Bercovici, D. & Karato, S., 2003. Theoretical analysis of shear localization in the lithosphere, in *Reviews in Mineralogy and Geochemistry: Plastic Deformation of Minerals and Rocks,* Vol. **51,** Chapter 13, pp. 387–420, eds Karato, S. & Wenk, H., Min. Soc. Am.

Bercovici, D. & Mulyukova, E., 2018. A continuum model for phase mixing and grain-damage relevant to tectonic plate boundary evolution, *Phys. Earth planet. Inter.,* **285,** 23–44.

Bercovici, D. & Mulyukova, E., 2021. Evolution and demise of passive margins through grain mixing and damage, *Proc. Natl. Acad. Sci.,* **118**(4), doi:10.1073/pnas.2011247118.

Bercovici, D. & Ricard, Y., 2012. Mechanisms for the generation of plate tectonics by two-phase grain-damage and pinning, *Phys. Earth planet. Inter.,* **202–203,** 27–55.

Bercovici, D. & Ricard, Y., 2013. Generation of plate tectonics with two-phase grain-damage and pinning: source–sink model and toroidal flow, *Earth planet. Sci. Lett.,* **365,** 275–288.

Bercovici, D. & Ricard, Y., 2016. Grain-damage hysteresis and plate-tectonic states, *Phys. Earth planet. Inter.,* **253,** 31–47.

Bercovici, D., Ricard, Y. & Schubert, G., 2001. A two-phase model of compaction and damage, 1. General theory, *J. geophys. Res.,* **106**(B5), 8887–8906.

Bercovici, D. & Skemer, P., 2017. Grain damage, phase mixing and plate-boundary formation, *J. Geodyn.,* **108,** 40–55.

Bercovici, D., Tackley, P.J. & Ricard, Y., 2015. The generation of plate tectonics from mantle dynamics, in *Treatise on Geophysics,* 2nd edn, Chapter 7.07, Vol. 7: Mantle Dynamics, pp. 271–318, ed. Schubert, G., Elsevier.

Bruijn, R.H. & Skemer, P., 2014. Grain-size sensitive rheology of orthopyroxene, *Geophys. Res. Lett.,* **41**(14), 4894–4903.

Canuto, C., Hussaini, M., Quarteroni, A. & Zang, T., 1988. *Spectral Methods in Fluid Dynamics,* Springer-Verlag.

Cross, A. & Skemer, P., 2017. Ultramylonite generation via phase mixing in high strain experiments, *J. geophys. Res.,* **122,** 1744–1759.

Cross, A.J., Olree, E., Couvy, H. & Skemer, P., 2020. How does viscosity contrast influence phase mixing and strain localization?, *J. geophys. Res.,* **125**(8), e2020JB020323, doi:10.1029/2020JB020323.

Engeln-Müllges, G. & Uhlig, F., 2013. *Numerical Algorithms with C,* Springer Science & Business Media.

Evans, B., Renner, J. & Hirth, G., 2001. A few remarks on the kinetics of static grain growth in rocks, *Int. J. Earth Sci. (Geol. Rundsch.),* **90,** 88–103.

Furusho, M. & Kanagawa, K., 1999. Reaction induced strain localization in a lherzolite mylonite from the hidaka metamorphic belt of Central Hokkaido, Japan, *Tectonophysics,* **313,** 411–432.

Handy, M.R., 1994. Flow laws for rocks containing two non-linear viscous phases: a phenomenological approach, *J. Struct. Geol.,* **16**(3), 287–301.

Hansen, L., Zimmerman, M., Dillman, A. & Kohlstedt, D., 2012. Strain localization in olivine aggregates at high temperature: a laboratory comparison of constant-strain rate and constant-stress boundary conditions, *Earth planet. Sci. Lett.,* **333–334**(0), 134–145.

Hansen, L.N., Cheadle, M.J., John, B.E., Swapp, S.M., Dick, H.J.B., Tucholke, B.E. & Tivey, M.A., 2013. Mylonitic deformation at the kane oceanic core complex: implications for the rheological behavior of oceanic detachment faults, *Geochem., Geophys., Geosyst.,* **14**(8), 3085–3108.

Hansen, L.N., Zimmerman, M.E. & Kohlstedt, D.L., 2011. Grain boundary sliding in San Carlos olivine: flow law parameters and crystallographic-preferred orientation, *J. geophys. Res.,* **116**(B8), doi:10.1029/2011JB008220b08201.

Herwegh, M., Linckens, J., Ebert, A., Berger, A. & Brodhag, S., 2011. The role of second phases for controlling microstructural evolution in polymineralic rocks: a review, *J. Struct. Geol.,* **33**(12), 1728–1750.

Hillert, M., 1965. On the theory of normal and abnormal grain growth, *Acta Metall.,* **13,** 227–238.

Hillert, M., 1988. Inhibition of grain growth by second-phase particles, *Acta Metall.,* **36**(12), 3177–3181.

Hirth, G. & Kohlstedt, D., 1995. Experimental constraints on the dynamics of the partially molten upper mantle: 2: deformation in the dislocation creep regime, *J. geophys. Res.,* **100,** 15 441–15 449.

Hirth, G. & Kohlstedt, D., 2003. Rheology of the upper mantle and the mantle wedge: a view from the experimentalists, in *Subduction Factor Mongraph,* Vol. **138,** pp. 83–105, ed. Eiler, J., Am. Geophys. Union.

Huang, H. & Seymour, B.R., 1996. The no-slip boundary condition in finite difference approximations, *Int. J. Numer. Methods Fluids,* **22**(8), 713–729.

Jin, D., Karato, S. & Obata, M., 1998. Mechanisms of shear localization in the continental lithosphere: Inference from the deformation microstructures of peridotites from the ivrea zone, northwestern italy, *J. Struct. Geol.,* **20,** 195–209.

Jung, H. & Karato, S., 2001. Effects of water on the size of recrystallized grains in olivine, *J. Struct. Geol.,* **23,** 1337–1344.

Karato, S., 1989. Grain growth kinetics in olivine aggregates, *Tectonophysics,* **168,** 255–273.

Karato, S., Toriumi, M. & Fujii, T., 1980. Dynamic recrystallization of olivine single crystals during high temperature creep, *Geophys. Res. Lett.,* **7,** 649–652.

Linckens, J., Bruijn, R.H. & Skemer, P., 2014. Dynamic recrystallization and phase mixing in experimentally deformed peridotite, *Earth planet. Sci. Lett.,* **388,** 134–142.

Linckens, J., Herwegh, M. & Müntener, O., 2015. Small quantity but large effect—how minor phases control strain localization in upper mantle shear zones, *Tectonophysics,* **643,** 26–43.

Linckens, J., Herwegh, M., Müntener, O. & Mercolli, I., 2011. Evolution of a polymineralic mantle shear zone and the role of second phases in the localization of deformation, *J. geophys. Res.,* **116**(B6), doi:10.1029/2010JB008119.

Manohar, P., Ferry, M. & Chandra, T., 1998. Five decades of the Zener equation, *ISIJ Int.,* **38**(9), 913–924.

McNamara, A., Karato, S. & van Keken, P., 2001. Localization of dislocation creep in the lower mantle: implications for seismic anisotropy, *Earth planet Sci. Lett.,* **911,** 85–99.

McNamara, A., van Keken, P. & Karato, S., 2002. Development of anisotropy in Earth's lower mantle due to solid-state deformation, *Nature,* **416,** 310–314.

Mulyukova, E. & Bercovici, D., 2017. Formation of lithospheric shear zones: effect of temperature on two-phase grain damage, *Phys. Earth planet. Inter.,* **270,** 195–212 .

Mulyukova, E. & Bercovici, D., 2018. A theoretical model for the evolution of microstructure in lithospheric shear zones, *Geophys. J. Int.,* **216**(2), 803–819 .

Mulyukova, E. & Bercovici, D., 2019. The generation of plate tectonics from grains to global scales: a brief review, *Tectonics,* **38**(12), 4058–4076 .

Mulyukova, E. & Bercovici, D., 2022. On the co-evolution of dislocations and grains in deforming rocks, *Phys. Earth planet. Inter.,* **328,** doi:10.1016/j.pepi.2022.106874.

Napolitano, M., Pascazio, G. & Quartapelle, L., 1999. A review of vorticity conditions in the numerical solution of the ζ-ψ equations, *Comput. Fluids,* **28**(2), 139–185 .

Olson, P., Yuen, D.A. & Balsiger, D., 1984a. Convective mixing and the fine structure of mantle heterogeneity, *Phys. Earth planet. Inter.,* **36**(3), 291–304 .

Olson, P., Yuen, D.A. & Balsiger, D., 1984b. Mixing of passive heterogeneities by mantle convection, *J. geophys. Res.,* **89**(B1), 425–436.

Patankar, S.V., 1980. *Numerical Heat Transfer and Fluid Flow,* Taylor and Francis.

Paterson, M. & Olgaard, D., 2000. Rock deformation tests to large shear strains in torsion, *J. Struct. Geol.,* **22**(9), 1341–1358.

Poirier, J., 1980. Shear localization and shear instability in materials in the ductile field, *J. Struct. Geol.,* **2,** 135–142.

Post, J. R.L., 1977. High-temperature creep of mt. burnet dunite, *Tectonophysics,* **42**(2–4), 75–110.

Ricard, Y. & Bercovici, D., 2009. A continuum theory of grain size evolution and damage, *J. geophys. Res.,* **114**(B1), doi:10.1029/2007JB005491.

Rozel, A., Ricard, Y. & Bercovici, D., 2011. A thermodynamically self-consistent damage equation for grain size evolution during dynamic recrystallization, *Geophys. J. Int.,* **184**(2), 719–728.

Skemer, P. & Hansen, L.N., 2016. Inferring upper-mantle flow from seismic anisotropy: an experimental perspective, *Tectonophysics,* **668,** 1–14.

Skemer, P., Warren, J.M., Kelemen, P.B. & Hirth, G., 2010. Microstructural and rheological evolution of a mantle shear zone, *J. Petrol.,* **51,** 43–53.

Smith, C.S., 1948. Grains, phases, and interfaces: an interpretation of microstructure, *Trans. A.I.M.E.,* **175,** 15–51.

Tackley, P.J., 2015. Mantle geochemical geodynamics, in *Treatise on Geophysics,* 2nd edn, Chapter 12, Vol. 7: Mantle Dynamics, pp. 521–585, Schubert, G., Elsevier.

Tasaka, M., Zimmerman, M.E. & Kohlstedt, D.L., 2017a. Rheological weakening of olivine + orthopyroxene aggregates due to phase mixing: 1. Mmechanical behavior, *J. geophys. Res.,* **122**(10), 7584–7596.

Tasaka, M., Zimmerman, M.E., Kohlstedt, D.L., Stünitz, H. & Heilbronner, R., 2017b. Rheological weakening of olivine + orthopyroxene aggregates due to phase mixing: Part 2. Microstructural development, *J. geophys. Res.,* **122**(10), 7597–7612.

Tasaka, M., Zimmerman, M.E. & Kohlstedt, D.L., 2020. Rheological weakening of olivine + orthopyroxene aggregates due to phase mixing: effects of orthopyroxene volume fraction, *J. geophys. Res.,* **125**(9), e2020JB019888,.

Van der Wal, D., Chopra, P., Drury, M. & FitzGerald, J., 1993. Relationships between dynamically recrystallized grain size and deformation conditions in experimentally deformed olivine rocks, *Geophys. Res. Lett.,* **20**(14), 1479–1482.

Warren, J.M. & Hirth, G., 2006. Grain size sensitive deformation mechanisms in naturally deformed peridotites, *Earth planet. Sci. Lett.,* **248**(1–2), 438–450.

White, S., Burrows, S., Carreras, J., Shaw, N. & Humphreys, F., 1980. On mylonites in ductile shear zones, *J. Struct. Geol.,* **2,** 175–187.

Wiesman, H., Zimmerman, M. & Kohlstedt, D., 2018. Laboratory investigation of mechanisms for phase mixing in olivine+ferropericlase aggregates, *Phil. Trans. R. Soc. A.,* **376**(2132),.

Zhang, G., Mei, S., Song, M. & Kohlstedt, D.L., 2017. Diffusion creep of enstatite at high pressures under hydrous conditions, *J. geophys. Res.,* **122**(10), 7718–7728.

Zhang, Z. & Karato, S.-I., 2021. The effect of pressure on grain-growth kinetics in olivine aggregates with some geophysical applications, *J. geophys. Res.,* **126**(2), e2020JB020886,.

Zhao, N., Hirth, G., Cooper, R.F., Kruckenberg, S.C. & Cukjati, J., 2019. Low viscosity of mantle rocks linked to phase boundary sliding, *Earth planet. Sci. Lett.,* **517,** 83–94.

APPENDIX: NUMERICAL APPROACH

The system of equations involves the coupled solution of the flow eqs (50) and (51) for the variables ψ and ω for given grain sizes R_i and volume fraction ϕ, and then using the resulting flow (eq. 49), deformation (eq. 53) and stress (eqs 39 and 55) fields to evolve R_i, r and ϕ via eqs (56)–(58). The essential algorithm is illustrated via flow chart in Fig. A1, and the details of how the governing equations are solved in each step are discussed later.

A1 Flow field

We employ a Cartesian geometry in the x–z plane, in a domain given by $x \in [-L, L]$ and $z \in [-1, 1]$, but assume the system is periodic in x over a fundamental wavelength of $2L$, as would be appropriate for torsion experiments. For our numerical model we assume $L = 5$. We thus assume all dependent variables can be represented by a discrete Fourier series such as

$$\Theta(x,z,t) = \sum_{k=-k_{max}}^{k_{max}} \check{\Theta}(k,z,t)e^{ikx} = \sum_{\mathsf{m}=-N_x/2}^{N_x/2} \check{\Theta}(\mathsf{m},z,t)e^{i\mathsf{m}\pi x/L}, \tag{A1}$$

where $k = \mathsf{m}\pi/L$ is the discrete wave number, N_x is the number of points in the x direction, Θ generically represents any of the dependent variables or forcing functions, and $\check{\Theta}$ is its discrete Fourier transform. With this mathematical framework, fast Fourier transforms can be readily used to go from quantities in fully physical space like $\Theta(x, z, t)$ to semi-spectral/semi-physical space $\check{\Theta}(k, z, t)$ via $\check{\Theta} = \mathsf{FFT}(\Theta)$ and $\Theta = \mathsf{FFT}^{-1}(\check{\Theta})$. In this case eqs (50) and (51) can be recast as

$$\left(\frac{\partial^2}{\partial z^2} - k^2\right)\check{\psi} = -\check{\omega} \tag{A2a}$$

$$\left(\frac{\partial^2}{\partial z^2} - k^2\right)\check{\omega} = \check{\mathcal{F}}_\omega, \tag{A2b}$$

where $\check{\psi} = \mathsf{FFT}(\psi)$, $\check{\omega} = \mathsf{FFT}(\omega)$, and $\check{\mathcal{F}}_\omega = \mathsf{FFT}(\mathcal{F}_\omega)$ in which

$$\mathcal{F}_\omega = -\mathcal{M}\nabla^2\omega - 2\nabla\mathcal{M}\cdot\nabla\omega + \Delta^*\mathcal{M}\,(\Omega_0 + \Delta^*\psi) + 4\frac{\partial^2\mathcal{M}}{\partial x\partial z}\frac{\partial^2\psi}{\partial x\partial z}. \tag{A3}$$

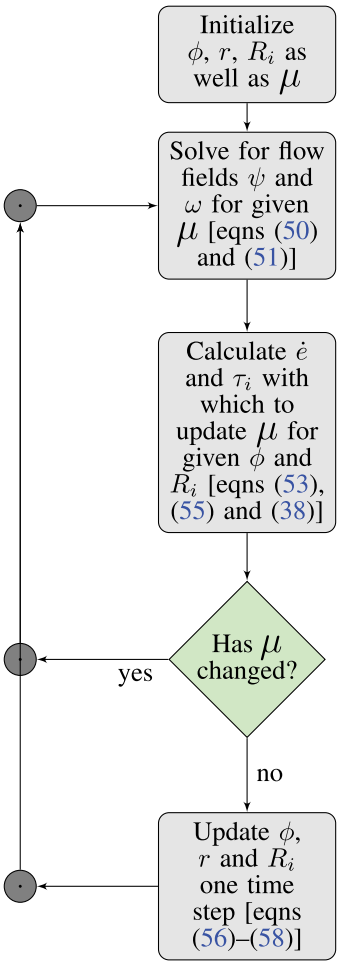

Figure A1. A flow chart for numerical solution of the coupled model.

Eq. (A2) represents now two coupled ordinary differential equations for a given wavenumber k. We can then apply a finite difference operator for the z domain divided into N_z points, such that, for example, for any given variable $\check{\Theta}$

$$\frac{\partial^2 \check{\Theta}}{\partial z^2} \approx \frac{\check{\Theta}_{j+1} - 2\check{\Theta}_j + \check{\Theta}_{j-1}}{\Delta z^2}, \tag{A4}$$

where the discrete position is given by $z_j = -1 + (j-1)\Delta z$, where $j \in [1, N_z]$, $\Delta z = 2/(N_z - 1)$, and thus $\check{\Theta}_j = \check{\Theta}(k, z_j, t)$.

The impermeable boundary condition (see the summary of boundary conditions given in eq. 52) leads to

$$\frac{\partial \psi}{\partial x} = \sum_k ik\check{\psi} e^{ikx} = 0 \ \text{ at } z = \pm 1 \tag{A5}$$

which is necessarily true for any k, and thus implies that

$$\check{\psi} = 0 \text{ at } z = \pm 1 \text{ or equivalently } \check{\psi}_j = 0 \text{ at } j = 1 \text{ and } N_z. \tag{A6}$$

With fixed stress at the top and bottom (again see eq. 52), all the boundary conditions are Dirichlet conditions on $\check{\psi}$ and $\check{\omega}$. Thus, substitution of eq. (A4) into eq. (A2) yields two tridiagonal matrix equations with simple boundary conditions implemented on the top and bottom rows of the matrices.

$$\begin{bmatrix} 1 & 0 & 0 & 0 & 0 & \dots & 0 \\ 1 & -\beta & 1 & 0 & 0 & \dots & 0 \\ 0 & 1 & -\beta & 1 & 0 & \dots & 0 \\ & & & \ddots & & & \\ 0 & \dots & 0 & 0 & 1 & -\beta & 1 \\ 0 & \dots & 0 & 0 & 0 & 0 & 1 \end{bmatrix} \begin{bmatrix} \check{\psi}_1 \\ \check{\psi}_2 \\ \check{\psi}_3 \\ \vdots \\ \check{\psi}_{N_z-1} \\ \check{\psi}_{N_z} \end{bmatrix} = -\Delta z^2 \begin{bmatrix} 0 \\ \check{\omega}_2 \\ \check{\omega}_3 \\ \vdots \\ \check{\omega}_{N_z-1} \\ 0 \end{bmatrix} \tag{A7a}$$

$$\begin{bmatrix} 1 & 0 & 0 & 0 & 0 & \dots & 0 \\ 1 & -\beta & 1 & 0 & 0 & \dots & 0 \\ 0 & 1 & -\beta & 1 & 0 & \dots & 0 \\ & & & \ddots & & & \\ 0 & \dots & 0 & 0 & 1 & -\beta & 1 \\ 0 & \dots & 0 & 0 & 0 & 0 & 1 \end{bmatrix} \begin{bmatrix} \check{\omega}_1 \\ \check{\omega}_2 \\ \check{\omega}_3 \\ \vdots \\ \check{\omega}_{N_z-1} \\ \check{\omega}_{N_z} \end{bmatrix} = \Delta z^2 \begin{bmatrix} -\check{\mathsf{M}}_1 \\ \check{\mathcal{F}}_{\omega 2} \\ \check{\mathcal{F}}_{\omega 3} \\ \vdots \\ \check{\mathcal{F}}_{\omega N_z-1} \\ -\check{\mathsf{M}}_{N_z} \end{bmatrix} \tag{A7b}$$

where $\mathsf{M} = \mathcal{M}/(1+\mathcal{M})$ from eq. (52), $\check{\mathsf{M}} = \mathsf{FFT}(\mathsf{M})$, and $\beta = 2 + k^2\Delta z^2$. Tridiagonal solutions are a traditional and simple finite difference technique since tridiagonal sparse matrix solvers, such as with the Thomas algorithm, are fast and easy to implement. We display these matrix equations for context relative to the discussion of the system with fixed velocity boundaries below.

The no-slip, fixed velocity boundary condition is, in semi-spectral space, still $\partial\check{\psi}/\partial z = 0$ at $z = \pm 1$, which is a Neumann condition. Both boundary conditions (i.e. also including $\check{\psi} = 0$ at $z = \pm 1$) are on $\check{\psi}$, and none are on $\check{\omega}$. The solution to this system using two elliptic equations as above is well known to be problematic in finite differences (Huang & Seymour 1996; Napolitano *et al.* 1999). For example, the no-slip condition can be used to approximate a condition on vorticity $\check{\omega}$, for example using the fact that $\check{\omega} = -\partial^2\check{\psi}/\partial z^2$ at $z = \pm 1$ with eq. (A4) to write $\check{\omega}(\pm 1) \approx -2\check{\psi}(\pm 1 \mp \Delta z)/\Delta z^2$. But, even for a linear system with fixed forcing $\check{\mathcal{F}}_\omega$, the solution is iterative—since the boundary condition on $\check{\omega}$ depends on interior values of $\check{\psi}$—rather than exact, as with Dirichlet conditions; this readily leads to numerical instabilities and lack of convergence (as learned by experience). A straight-forward solution to this conundrum is to just abandon the tridiagonal solution method, and to combine (A2) into one fourth-order biharmonic equation

$$\left(\frac{\partial^2}{\partial z^2} - k^2\right)^2 \check{\psi} = -\check{\mathcal{F}}_\omega. \tag{A8}$$

Using the discretization operator eq. (A4), this eventually leads to the single pentadiagonal system

$$\begin{bmatrix} 1 & 0 & 0 & 0 & 0 & 0 & \dots & 0 \\ -2\beta & 1+\gamma & -2\beta & 1 & 0 & 0 & \dots & 0 \\ 1 & -2\beta & \gamma & -2\beta & 1 & 0 & \dots & 0 \\ 0 & 1 & -2\beta & \gamma & -2\beta & 1 & \dots & 0 \\ & & & & \ddots & & & \\ 0 & \dots & 0 & 1 & -2\beta & \gamma & -2\beta & 1 \\ 0 & \dots & 0 & 0 & 1 & -2\beta & 1+\gamma & -2\beta \\ 0 & \dots & 0 & 0 & 0 & 0 & 0 & 1 \end{bmatrix} \begin{bmatrix} \check{\psi}_1 \\ \check{\psi}_2 \\ \check{\psi}_3 \\ . \\ \vdots \\ . \\ \check{\psi}_{N_z-1} \\ \check{\psi}_{N_z} \end{bmatrix} = -\Delta z^2 \begin{bmatrix} 0 \\ \check{\mathcal{F}}_{\omega 2} \\ \check{\mathcal{F}}_{\omega 3} \\ . \\ \vdots \\ . \\ \check{\mathcal{F}}_{\omega N_z-1} \\ 0 \end{bmatrix}, \tag{A9}$$

where $\gamma = 6 + 4k^2\Delta z^2 + k^4\Delta z^4$. Note that while the top and bottom rows of the matrix incorporate the impermeable boundary condition $\check{\psi} = 0$, the 2nd from the top and the 2nd to last rows incorporate the no-slip condition $\partial\check{\psi}/\partial z = 0$ to approximate 4th order derivatives in the biharmonic equation, which leads to the diagonal terms there being $1+\gamma$ instead of γ as elsewhere at other interior points. This system can be solved with fast pentadiagonal solvers (Engeln-Müllges & Uhlig 2013, chapter 4), which can be (from our experience) 50 times faster for large matrices ($N_z > 100$) than standard matrix solutions (e.g. the MATLAB operation x = A\b to solve Ax=b despite its automatic sparse matrix solutions), provided superfluous conditional tests (e.g. checking for matrix symmetry) are removed and the five diagonals are passed directly as vectors (rather than with the entire pentadiagonal matrix, for which the diagonals then need to be extracted anyway).

The non-linearity in the solution to the flow equations arises from the forcing function $\mathcal{F}_\omega$. This function is non-linear not only by dint of products between derivatives of the normalized viscosity $\mathcal{M}$ and derivatives of ω and ψ, but also because $\mathcal{M}$ is itself a non-linear function of R_i and the flow fields through evaluation of τ_i and $\dot{e}$. Thus to facilitate stable solutions, we solve the flow equations [either eq. (A7) or eq. (A9) depending on boundary conditions)] first for a given $\mathcal{M}$ until ω converges (since it has more power at high wave-numbers k than does ψ, and thus needs better resolution). Then $\mathcal{M}$ is updated given the flow field (for which $\dot{e}$, τ_i and τ are re-evaluated) but for a given ϕ and R_i at that time step, after which the flow solutions are determined again for the new $\mathcal{M}$. This double embedded iteration is repeated until $\mathcal{M}$ converges, after which the flow solutions are used to updated ϕ, r and R_i to the next time step and the process is repeated (see Fig. A1).

Finally, note that in the process of transforming non-linear functions such as $\mathcal{F}_\omega$ and $\mathsf{M} = \mathcal{M}/(1+\mathcal{M})$ (used in the fixed stress boundary condition) to spectral or Fourier space (i.e. from x to k space) it is necessary to dealias the resulting transformed quantities such as $\check{\mathcal{F}}_\omega$, $\check{\mathsf{M}}$, etc. This is simply done by applying a low-pass filter that effectively pads all transformed dependent variables such as $\check{\psi}$ and $\check{\omega}$ with zeros for (typically) half the highest wavenumber modes; i.e., the variables are non-zero for $|k| \le \pi N_x/4$ and zero for $\pi N_x/4 < |k| \le \pi N_x/2$, which can be done with a simple box-car type filter. After non-linear products are taken in physical space, and then Fourier transformed, their higher wavenumber modes for $|k| > \pi N_x/4$ are filled by wave-wave products rather than those products deposited at low wavenumbers causing aliasing; but then these modes are simply zeroed out again to be consistent with the dependent variables' resolution in spectral space. In essence, space is made (in k space) to place wave–wave products arising from non-linearities—rather than letting them fall into the wrong aliased modes—after which they're eliminated. However using half the modes is appropriate strictly for quadratic non-linearities, and in principle one would zero out more modes for higher order non-linearities. But, there is a point of diminishing returns where one is keeping

so few non-zero modes that, although aliasing is reduced, the solutions are too crudely resolved. From empirical approaches (i.e. trial and error), keeping half the modes typically works best and is reasonably conservative (see also Canuto *et al*. 1988).

A1.1 A short note on the solution for stress

The viscosity μ, which determines $\mathcal{M}$ in the flow field equations, depends on the strain rate $\dot{e}$, given by eq. (53), and the stress τ_i in phase i, which is the solution to eq. (55), repeated here for exposition:

$$\tau_i^n + \frac{\tau_i}{R_i^m} - 2\dot{e} = 0. \tag{A10}$$

As stated earlier, for $n = 1$, 2 or 3 there is a simple analytic solution for τ_i. For the laboratory inferred $n = 3.5$ or any non-integer value of n, τ_i must be solved numerically. Given that each phases' stress must be solved at every gridpoint at each time step, the numerical solution of eq. (A10) by standard means like Newton–Raphson or bisection can be costly and slow. Here we explain a fast solution that uses accurate approximate analytic solutions with very few iterations. Specifically, we start with a good initial guess solution that is the harmonic sum of diffusion and dislocation creep stresses:

$$\tilde{\tau}_i = \left(\frac{1}{(2\dot{e})^{1/n}} + \frac{1}{2R_i^m \dot{e}} \right)^{-1} \tag{A11}$$

which is reasonably accurate for R_i significantly different from unity. We then substitute $\tau_i \approx \tilde{\tau}_i(1 + s)$ into eq. (A10) and expand the relation to second order in s to yield

$$\left(\tfrac{1}{2}n(n-1)\tilde{\tau}_i^n\right)s^2 + \left(n\tilde{\tau}_i^n + \tilde{\tau}_i/R_i^m\right)s + \left(\tilde{\tau}_i^n + \tilde{\tau}_i/R_i^m - 2\dot{e}\right) = 0 \tag{A12}$$

with which we can determine s to reasonable accuracy. Repeating the procedure but replacing $\tilde{\tau}_i$ with the new solution $\tau_i = \tilde{\tau}_i(1 + s)$ leads to a more accurate solution. A single repetition is sufficient for solutions accurate to 10^{-6} relative error (i.e. relative to exact solutions) for R_i far from unity. For R_i that is $O(1)$, one extra repetition (three iterations total, starting with the initial guess $\tilde{\tau}_i$) allows for equally accurate solutions. We generally just apply three iterations for all cases so that no convergence test need be applied at every gridpoint, which is otherwise cumbersome. This method is generally considerably faster than standard numerical solutions and even root-finding routines when eq. (A10) can be expressed as a polynomial.

A2 Grain-mixing diffusion

The numerical solution of the grain-mixing diffusion eq. (56), which is used to update ϕ, uses a semi-spectral, finite-difference, semi-impicit time integration for a non-linear (mostly) parabolic-like equation. For simplicity of notation we rewrite eq. (56) as

$$\frac{D\phi}{Dt} = \frac{\partial}{\partial x}\left((\Lambda - \Lambda_\mathrm{N})\frac{\partial\phi}{\partial x}\right) + \frac{\partial}{\partial z}\left((\Lambda + \Lambda_\mathrm{N})\frac{\partial\phi}{\partial z}\right) - \frac{\partial}{\partial x}\left(\Lambda_\mathrm{S}\frac{\partial\phi}{\partial z}\right) - \frac{\partial}{\partial z}\left(\Lambda_\mathrm{S}\frac{\partial\phi}{\partial x}\right), \tag{A13}$$

where $\Lambda_l = \alpha\chi\tau_l$ and $l = \mathrm{S}, \mathrm{N}$ or nothing. We then separate the Λ_l into uniform and varying portions according to $\Lambda_l = \bar{\Lambda}_l + \Lambda_l'(x, z, t)$ where $\bar{\Lambda}_l$ can, for example, be the mean, maximum or minimum value of Λ_l, although we typically use the maximum value, which yields the most stable solutions. This separation allows us to express eq. (A13) in terms of linear operators on its left side, and all non-linear products on its right-hand side:

$$\begin{aligned}\frac{\partial\phi}{\partial t} + \Omega_0 z\frac{\partial\phi}{\partial x} - \bar{\Lambda}\nabla^2\phi + \bar{\Lambda}_\mathrm{N}\Delta^*\phi + 2\bar{\Lambda}_\mathrm{S}\frac{\partial^2\phi}{\partial x\partial z} &= \frac{\partial\psi}{\partial z}\frac{\partial\phi}{\partial x} - \frac{\partial\psi}{\partial x}\frac{\partial\phi}{\partial z} + \Lambda'\nabla^2\phi - \Lambda_\mathrm{N}'\Delta^*\phi - 2\Lambda_\mathrm{S}'\frac{\partial^2\phi}{\partial x\partial z} \\ &+ \left(\frac{\partial(\Lambda' - \Lambda_\mathrm{N}')}{\partial x} - \frac{\partial\Lambda_\mathrm{S}'}{\partial z}\right)\frac{\partial\phi}{\partial x} + \left(\frac{\partial(\Lambda' + \Lambda_\mathrm{N}')}{\partial z} - \frac{\partial\Lambda_\mathrm{S}'}{\partial x}\right)\frac{\partial\phi}{\partial x} = \mathcal{F}_\phi,\end{aligned} \tag{A14}$$

where we have used the expression for velocity from eq. (49). When the discrete Fourier representation is used, the above equation becomes

$$\frac{\partial\check{\phi}}{\partial t} + ik\Omega_0 z\check{\phi} - \bar{\Lambda}\left(\frac{\partial^2}{\partial z^2} - k^2\right)\check{\phi} - \bar{\Lambda}_\mathrm{N}\left(\frac{\partial^2}{\partial z^2} + k^2\right)\check{\phi} + ik2\bar{\Lambda}_\mathrm{S}\frac{\partial\check{\phi}}{\partial z} = \check{\mathcal{F}}_\phi \tag{A15}$$

which, when finite differenced in time with a semi-implicit scheme becomes

$$\begin{aligned}&\check{\phi}^{\mathrm{n}+1} + \tfrac{\Delta t}{2}\left[ik\Omega_0 z\check{\phi}^{\mathrm{n}+1} - \bar{\Lambda}\left(\frac{\partial^2}{\partial z^2} - k^2\right)\check{\phi}^{\mathrm{n}+1} - \bar{\Lambda}_\mathrm{N}\left(\frac{\partial^2}{\partial z^2} + k^2\right)\check{\phi}^{\mathrm{n}+1} + ik2\bar{\Lambda}_\mathrm{S}\frac{\partial\check{\phi}^{\mathrm{n}+1}}{\partial z}\right] \\ &= \check{\phi}^{\mathrm{n}} - \tfrac{\Delta t}{2}\left[ik\Omega_0 z\check{\phi}^{\mathrm{n}} - \bar{\Lambda}\left(\frac{\partial^2}{\partial z^2} - k^2\right)\check{\phi}^{\mathrm{n}} - \bar{\Lambda}_\mathrm{N}\left(\frac{\partial^2}{\partial z^2} + k^2\right)\check{\phi}^{\mathrm{n}} + ik2\bar{\Lambda}_\mathrm{S}\frac{\partial\check{\phi}^{\mathrm{n}}}{\partial z}\right] + \check{\mathcal{F}}_\phi{}^{\mathrm{n}} = \check{\mathcal{H}}_\phi{}^{\mathrm{n}},\end{aligned} \tag{A16}$$

where $\check{\mathcal{F}}_\phi$ is also dealiased, and n indicates the time step of size Δt (which is itself determined with a standard CFL condition). The insulating (zero flux) boundary condition from eq. (14) can be expressed as

$$\frac{\partial\phi}{\partial z} = \frac{\Lambda_\mathrm{S}}{\Lambda + \Lambda_\mathrm{N}}\frac{\partial\phi}{\partial x} = \frac{\partial\phi}{\partial x} + \frac{\Lambda_\mathrm{S} - \Lambda + \Lambda_\mathrm{N}}{\Lambda + \Lambda_\mathrm{N}}\frac{\partial\phi}{\partial x} = \frac{\partial\phi}{\partial x} + h_\phi \tag{A17}$$

which in semi-spectral (k, z) space becomes

$$\frac{\partial \check{\phi}}{\partial z} = ik\phi + \check{h}_\phi \tag{A18}$$

where $\check{h}_\phi$ is dealiased like other non-linear functions. Eq. (A16) is then discretized in space as per eq. (A4), but where eq. (A18) is used to evaluate the 2nd order derivatives in eq. (A16) at the boundaries. The whole discretized system is expressed with a tridiagonal matrix operator and solved accordingly, similarly to the method discussed above (Section A1), although the details are not shown here.

A3 Grain damage

The evolution equations for grain sizes R_i and interface roughness r, eqs (57) and (58), are solved in physical space; we rewrite these equations as

$$\frac{\partial r}{\partial t} = \mathcal{A}_r + \mathcal{F}_r \tag{A19a}$$

$$\frac{\partial R_i}{\partial t} = \mathcal{A}_{R_i} + \mathcal{F}_{R_i}, \tag{A19b}$$

where

$$\mathcal{A}_r = -\frac{\partial \psi}{\partial x}\frac{\partial r}{\partial z} + \left(-\Omega_0 z + \frac{\partial \psi}{\partial z}\right)\frac{\partial r}{\partial x} \tag{A20a}$$

$$\mathcal{A}_{R_i} = -\frac{\partial \psi}{\partial x}\frac{\partial R_i}{\partial z} + \left(-\Omega_0 z + \frac{\partial \psi}{\partial z}\right)\frac{\partial R_i}{\partial x} \tag{A20b}$$

are the non-linear advection terms, and

$$\mathcal{F}_r = \tfrac{\eta \mathcal{C}_I}{q r^{q-1}} - \mathcal{D}_I \eta^\ell r^2 \tau \left(2\dot{e} + \tfrac{1}{2}\left[\sqrt{\Lambda - \Lambda_N}\tfrac{\partial \phi}{\partial x} - \sqrt{\Lambda + \Lambda_N}\tfrac{\partial \phi}{\partial z}\right]^2\right) \tag{A21a}$$

$$\mathcal{F}_{R_i} = \tfrac{\mathcal{C}_i}{p R_i^{p-1}}\mathcal{Z}_i - \mathcal{D}_i R_i^2 \tau_i^{n+1} \mathcal{Z}_i^{-1} \tag{A21b}$$

combine the healing (coarsening) and damage (comminution) terms for both equations. The evaluation of derivatives in x are done spectrally, with Fourier transforms, while those in z are done spatially with 2nd-order finite difference approximations. We can approximate (A19) with semi-implicit finite differences in time as

$$r^{n+1} = r^n + \Delta t\left[\mathcal{A}_r^n + \mathcal{F}_r\left(\tfrac{r^{n+1}+r^n}{2}\right)\right] = r^n + \Delta t\left[\mathcal{A}_r^n + \mathcal{F}_r(r^n) + \tfrac{1}{2}(r^{n+1} - r^n)\tfrac{\partial \mathcal{F}_r}{\partial r}\Big|_{r^n}\right] \tag{A22a}$$

$$R_i^{n+1} = R_i^n + \Delta t\left[\mathcal{A}_{R_i}^n + \mathcal{F}_{R_i}\left(R_i^n\right) + \tfrac{1}{2}\left(R_i^{n+1} - R_i^n\right)\tfrac{\partial \mathcal{F}_{R_i}}{\partial R_i}\Big|_{R_i^n}\right], \tag{A22b}$$

where we write the whole of $\mathcal{A}_r$ and $\mathcal{A}_{R_i}$ explicitly since terms with $\frac{\partial r}{\partial x}$ and $\frac{\partial R_i}{\partial x}$ need to be treated explicitly, but we treat $\mathcal{F}_r$ and $\mathcal{F}_{R_i}$ semi-implicitly with Taylor expansions to linearize non-linear source terms (see Patankar 1980). eqs (A22) can be re-organized accordingly to give an expression to update r and R_i to a new time-step

$$r^{n+1} = r^n + \Delta t\frac{\mathcal{A}_r^n + \mathcal{F}_r(r^n)}{1 - \frac{1}{2}\Delta t \partial \mathcal{F}_r/\partial r\big|_{r^n}} \tag{A23a}$$

$$R_i^{n+1} = R_i^n + \Delta t\frac{\mathcal{A}_{R_i}^n + \mathcal{F}_{R_i}(R_i^n)}{1 - \frac{1}{2}\Delta t \partial \mathcal{F}_{R_i}/\partial R_i\big|_{R_i^n}} \tag{A23b}$$

which thus completes the full coupled integration of the system of equations by one time step.